

Solar Cruiser Disturbance Torque Estimation and Predictive Momentum Management

Ping-Yen Shen^a, Ryan J. Caverly^{a,*}

^a*Department of Aerospace Engineering and Mechanics, University of Minnesota, Twin Cities, 110 Union St. SE, Minneapolis, MN, 55455, USA*

Abstract

This paper presents a novel disturbance-torque-estimation-augmented model predictive control (MPC) framework to perform momentum management on NASA's Solar Cruiser solar sail mission. Solar Cruiser represents a critical step in the advancement of large-scale solar sail technology and includes the innovative use of an active mass translator (AMT) and reflectivity control devices (RCDs) as momentum management actuators. The coupled nature of these actuators has proven challenging in the development of a robust momentum management controller. Recent literature has explored the use of MPC for solar sail momentum management with promising results, although exact knowledge of the disturbance torques acting on the solar sail was required. This paper amends this issue through the use of a Kalman filter to provide real-time estimation of unmodeled disturbance torques. Furthermore, the dynamic model used in this paper incorporates key fidelity enhancements compared to prior work, including the Solar Cruiser's four-reaction-wheel assembly and the offset between its center of mass and center of pressure. Simulation results demonstrate that the proposed policy successfully manages angular momentum growth under slew maneuvers that exceed the operational envelope of the current state-of-the-art method. The inclusion of the disturbance torque estimate is shown to greatly improve the reliability and performance of the proposed MPC approach. This work establishes a new benchmark for Solar Cruiser's momentum management capabilities and paves the way for MPC-based momentum management of other solar sails making use of an AMT and/or RCDs.

Keywords: Solar Sails, Momentum Management, Model Predictive Control (MPC), Disturbance Estimation, Kalman Filtering, Solar Cruiser

1. Introduction

Solar sails have the potential to remove the space exploration limits imposed by traditional propellant-based propulsion, thus unlocking a wide range of missions previously unattainable by conventional spacecraft (Macdonald and McInnes, 2011; Berhet et al., 2024; Farres, 2023; Miller et al., 2022; Farrés et al., 2019). Effectively leveraging the propulsion induced by solar radiation pressure (SRP) and unlocking solar sail travel requires both advancements in the design and deployment of large sail structures (Vatankhahghadam and Damaren, 2021; Hibbert and Jordaan, 2021; Huang et al., 2021) and the concurrent development of advanced control technology (Chen et al., 2023; Inness et al., 2024, 2023). NASA's Solar Cruiser, which features a massive sail membrane area exceeding 1,600 m², is designed to pioneer next-generation space exploration capabilities and enable groundbreaking heliophysics observations (Johnson et al., 2019; Johnson and Curran, 2020; Johnson et al., 2022; Pezent et al., 2021).

Generating the required propulsion from SRP necessitates precise pointing via attitude control. However, the operation of such large, flexible structures introduces significant control challenges (Boni et al., 2023; Fu and Eke, 2015; Firuzi and Gong, 2018). Imperfect sail shapes and structural flexibility induce persistent disturbance torques (Gauvain and Tyler, 2023) that cause angular momentum accumulation within the onboard reaction wheels (RWs). This necessitates effective momentum management to desaturate the RWs and prevent a loss of attitude control authority. Conventional momentum management methods, such as thrusters or magnetic torquers, are unsuitable for long-term, interplanetary, deep-space missions because they either require fuel or are limited to operations near Earth's magnetic field. Innovative actuation methodologies have been developed to adapt to solar sail missions (Wie, 2004;

*Corresponding author: Tel.: +1-612-625-8000

Email address: rcaverly@umn.edu (Ryan J. Caverly)

Orphee et al., 2018; Lee et al., 2025). On Solar Cruiser, momentum management is achieved using two specialized actuators: the active mass translator (AMT) and reflectivity control devices (RCDs) (Inness et al., 2023).

Solar Cruiser's AMT functions as an internal mechanism that shifts the spacecraft's center of mass (CM) relative to the sail's center of pressure (CP) in a plane parallel to the sail surface. This controllable motion produces SRP-induced torques to counteract disturbance torques in the pitch and yaw axes (torques within the plane of the sail) and unload RW angular momentum (Orphee et al., 2018). The RCDs consist of thin-film membrane pairs, positioned near the tip of each sail boom, set at fixed opposite inclination angles (Heaton et al., 2023). These devices generate a net roll-axis torque (torque normal to the plane of the sail) by selectively varying the reflectivity of the appropriate RCD membranes via applied voltages, resulting from an imbalance in the differential SRP forces. A key operational constraint of RCDs is their binary actuation, as they function in an on-off manner, capable only of generating either zero torque or a fixed-magnitude torque in the positive or negative roll direction.

The current design of Solar Cruiser employs a decoupled momentum management strategy, where individual-channel threshold-activated proportional-integral-derivative (PID) controllers command the AMT's two axes and a threshold-based strategy governs the RCDs (Tyler et al., 2023). While this approach has been shown to manage angular momentum successfully (Inness et al., 2023), its reliance on purely reactive, threshold-based methods, as well as its neglect of coupled interactions between the AMT motion, RCD input, and the resulting effect on motion in all three axes are significant limitations. Specifically, the inability of this state-of-the-art method to optimize the AMT and RCD inputs in a coordinated fashion and proactively prevent RW angular momentum saturation limits its performance under larger slew maneuvers.

The increasing computational capability of modern flight hardware has established model predictive control (MPC) as a viable and practical option for spacecraft attitude determination and control (Di Cairano and Kolmanovsky, 2018; Eren et al., 2017; Caverly et al., 2020; Halverson et al., 2025). MPC is a control methodology that solves an online optimization problem to determine the optimal future sequence of control actions, simultaneously enforcing constraints on both state trajectories and actuator limits, with a receding-horizon. The properties of solar sail dynamics are particularly amenable to this strategy. The low magnitude of SRP ensures slew maneuvers are inherently slow and result in smooth system dynamics. Moreover, MPC has the potential to enforce the hard constraints associated with RW saturation and optimally allocate the limited control authority associated solar sail actuators through state and input constraints. This combination of long time scales available for onboard processing and the need to enforce state and input constraints make MPC an ideal choice for the intricate task of solar sail momentum management.

Prior work by Shen and Caverly (2025b) developed MPC-based momentum management strategies tailored for solar sails equipped with an AMT and RCDs. They developed a dynamic model that captured key features of the AMT movement, including the resultant time-varying changes in the spacecraft's CM and moment of inertia matrix. The MPC policy developed in the work of Shen and Caverly (2025b) leveraged its optimization capabilities to handle the actuator constraints and requirements, including the enforcement of on-off RCD actuation and AMT motion rate limits, all while incorporating tuning parameters designed to adjust the trade-off between system performance and control effort. For real-time onboard implementation, the MPC formulation was posed as a quadratic program (QP), which guarantees fast and robust convergence suitable for the short processing cycles required by the flight computer. The work of Shen and Caverly (2025a) further examined the critical balance between model fidelity and computational cost when implementing the MPC policy developed by Shen and Caverly (2025b) to determine feasibility for real-time implementation. However, these MPC implementations both make an unrealistic assumption that exact knowledge of the disturbance torque acting on the solar sail is available for use within MPC's prediction model. This is a significant assumption that limits practical implementation of the MPC policy proposed by Shen and Caverly (2025b), as unpredictable shape deformation of the solar sail and temporal changes in the sail's optical properties make it virtually impossible to accurately predict disturbance torques from analytical models (Wang et al., 2025; Gauvain and Tyler, 2023). The use of an inaccurate torque model within the MPC framework significantly degrades momentum management performance, negating the purported benefits of the MPC momentum management policy. Another practical limitation of the work of Shen and Caverly (2025b,a) is that their implementations assume that the solar sail is equipped with three RWs aligned with the principal axes of its body-fixed frame. Many spacecraft, including Solar Cruiser, have a 4-RW assembly for redundancy and increased performance, which precludes the use of the methods developed by Shen and Caverly (2025b,a). Furthermore, the implementation in the work of Shen and Caverly (2025b) assumed that the RWs remained in the same plane as the solar sail's CP, which is not representative of Solar Cruiser's geometry.

To overcome the limitations of prior work, this paper presents a novel MPC-based momentum management policy that incorporates disturbance torque estimation and a 4-RW assembly tailored for the Solar Cruiser mission. A Kalman filter framework is used to estimate the unmodeled disturbance torques and system model errors in real time, thus

enhancing the predictive capability of the MPC. Similar Kalman-filtering approaches have been used in the literature to estimate unknown parameters or terms within a system model (Zenere and Zorzi, 2018; Woodbury and Junkins, 2010; Hayes and Caverly, 2025; Ahmed et al., 2024). For example, Hayes and Caverly (2025) used a Kalman filter to estimate the unknown atmospheric density of a satellite during an orbital reentry, while Ahmed et al. (2024) estimated the unknown wind acting on a small uncrewed air vehicle. Solar Cruiser’s 4-RW assembly is accounted for within the proposed MPC implementation through the use of the commonly-used pseudo-inverse RW allocation approach (Leve et al., 2015; Markley and Crassidis, 2014). This provides the MPC prediction model with accurate knowledge of the dynamics of each individual RW, allowing for their operation to be constrained within their saturation limits.

This paper presents three key contributions relative to the state-of-the-art in solar sail momentum management, including prior work on MPC-based methods by Shen and Caverly (2025b,a). The first contribution is a robust MPC momentum management formulation that uses a Kalman filter to estimate unknown disturbance torques acting on the solar sail. To the best of the knowledge of the authors, this is the first realistically-implementable momentum management policy for a solar sail equipped with an AMT and RCD that outperforms the method of Tyler et al. (2023). The second contribution is the incorporation of a 4-RW assembly within an MPC-based momentum management policy. To the best of the knowledge of the authors, this is the first MPC-based momentum management policy to consider a realistic 4-RW assembly. The third contribution is an assessment of the proposed momentum management policy in a realistic simulation of Solar Cruiser’s dynamics, where its CM is located a distance from the sail plane and non-ideal SRP forces are considered. Both these effects are meaningful when considering Solar Cruiser’s dynamics, as they result in substantial coupling between axes, yet they were not considered in the prior work of Shen and Caverly (2025b).

Details of the nonlinear system dynamics of Solar Cruiser, the 4-RW control allocation algorithm, and the momentum management actuators are presented in Section 2. This section also provides the linearized dynamic model used in the Kalman filter and MPC frameworks. The Kalman filter formulation is presented in Section 3, providing details of how the unmeasurable disturbance torques are estimated. The MPC formulation is presented in Section 4, detailing the implementation of estimation-prediction framework and the incorporation of the 4-RW assembly into the MPC prediction model. Numerical simulation results are presented in Section 5, validating the performance of the proposed estimation-augmented MPC with comparisons to Solar Cruiser’s state-of-the-art momentum management method (Tyler et al., 2023). Results in this section are also presented that demonstrate the effect of actuation thresholds within the proposed momentum management policy on actuation efficiency and observability of the roll-axis disturbance torque.

2. Attitude Dynamics and Control Actuation

NASA’s Solar Cruiser uses AMT and RCDs as its momentum management actuators (Inness et al., 2023). The AMT changes the relative alignment of the CM and CP such that the SRP force acting on the CP results in a corresponding torque about the CM. Moving the AMT and appropriately placing the CM/CP offset results in a controllable moment that unloads the accumulated RW angular momentum. However, the moment of inertia matrix changes when the AMT moves and the mass distribution of the sailcraft changes. The dynamics are thus coupled with the AMT translation. This section presents the dynamics and control of the sailcraft, starting with important notation and proceeding with its attitude dynamics, the RW attitude control law, and details regarding the momentum management control actuation.

2.1. Notation

The identity matrix of dimension $n \times n$ is denoted as $\mathbf{1}_{n \times n}$, while an $n \times m$ matrix of zeros is given by $\mathbf{0}_{n \times m}$. Physical vectors are denoted as \underline{v} . Reference frame \mathcal{F}_a is defined by three orthonormal, dextral physical basis vectors $\underline{a}^1, \underline{a}^2$, and \underline{a}^3 . The physical vector \underline{v} resolved in \mathcal{F}_a is denoted as $\mathbf{v}_a = [v_{a1} \quad v_{a2} \quad v_{a3}]^\top$. The position of point q relative to point z is given by \underline{r}_a^{qz} , which is expressed as \mathbf{r}_a^{qz} when resolved in reference frame \mathcal{F}_a . The cross product operator $(\cdot)^\times$ is used to compute the cross product of two vectors resolved in a particular reference frame. For example, $\underline{u} \times \underline{v}$ resolved in \mathcal{F}_a is computed as $\mathbf{u}_a^\times \mathbf{v}_a$, where

$$\mathbf{u}_a^\times = \begin{bmatrix} 0 & -u_{a3} & u_{a2} \\ u_{a3} & 0 & -u_{a1} \\ -u_{a2} & u_{a1} & 0 \end{bmatrix},$$

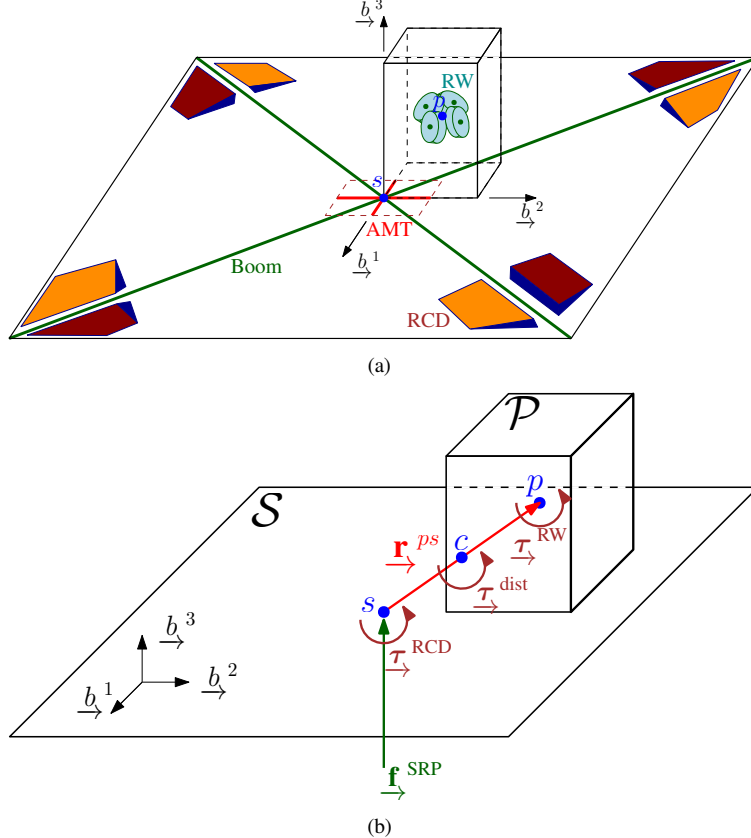


Figure 1: Depictions of the Solar Cruiser model used in this paper (not drawn to scale) highlighting (a) its attitude control and momentum management actuators, including four RWs (light blue), AMT (red) and RCDs (brown and orange); and (b) the definition of key bodies and, such as the sail \mathcal{S} with CM s (also the CP of the entire sailcraft) and the bus \mathcal{P} with CM p , as well as the entire sailcraft's CM c .

and $\mathbf{u}_a = [u_{a1} \ u_{a2} \ u_{a3}]^\top$.

The direction cosine matrix (DCM) \mathbf{C}_{ba} describes the attitude of reference frame \mathcal{F}_b relative to reference frame \mathcal{F}_b . While different attitude parameterizations can be used to describe a DCM, Euler-angle sequences are used in this work due to their ease of physical interpretation and the lack of any large-angle maneuvers that would potentially result in a kinematic singularity. The DCM can be used to express a physical vector in different reference frames. For example, $\mathbf{v}_b = \mathbf{C}_{ba}\mathbf{v}_a$.

Within the proposed MPC policy, the subscript $j|t_k$ is used to refer to system states or inputs j time steps ahead of the current time step t_k .

2.2. Solar Cruiser Attitude Dynamics

Following the approach of Shen and Caverly (2025b) and as illustrated in Fig. 1, Solar Cruiser's sail is modeled as a thin flat plate (denoted as \mathcal{S}) and a rigid rectangular bus (denoted as \mathcal{P}). The nonlinear rigid-body attitude dynamics of a solar sail incorporating the AMT translation as a control input were derived by Shen and Caverly (2025b), including the time-dependent moment of inertia matrix corresponding to the AMT position. It is assumed that the RWs are colocated at the CM of the bus (point p) since the dimension of the sail \mathcal{S} is much greater than the dimension of the bus \mathcal{P} . As shown in Fig. 1(a), the sailcraft body frame \mathcal{F}_b is defined with \mathcal{b}^3 pointing through the normal (roll) axis of the sail, and \mathcal{b}^2 , \mathcal{b}^1 pointing within the plane of the sail and representing the pitch and yaw axes, respectively. The moment of inertia matrix relative to the sailcraft's CM (point c) is defined as

$$\mathbf{J}_b^{Bc}(t) = \mathbf{J}_b^{\mathcal{S}s} + \mathbf{J}_b^{\mathcal{P}p} - \frac{m_p^3 + m_s^3}{(m_p + m_s)^2} \mathbf{r}_b^{ps^x}(t) \mathbf{r}_b^{ps^x}(t),$$

where m_s and m_p are the masses of the sail and the bus, respectively, \mathbf{J}_b^{Ss} and \mathbf{J}_b^{Pp} are the nominal moment of inertia matrices of the sail and bus relative to each of their own CMs (points s and p), respectively, and the position $\mathbf{r}_b^{ps}(t) = [r_{b1}^{\text{AMT}}(t) \ r_{b2}^{\text{AMT}}(t) \ r_{b3}^{ps}]^\top$ contains the controllable AMT positions $r_{b1}^{\text{AMT}}(t)$ and $r_{b2}^{\text{AMT}}(t)$. These AMT positions are actuated via the red linear actuators visualized in Fig. 1(a). The constant component r_{b3}^{ps} represents the constant offset distance in the $\overset{\rightarrow}{b^3}$ sail-normal direction between the CM of the sail and the CM of the bus.

Let \mathcal{F}_a , defined by basis vectors $\overset{\rightarrow}{a^1}, \overset{\rightarrow}{a^2}, \overset{\rightarrow}{a^3}$, be an inertial reference frame. The solar sail attitude dynamics with mass translation are defined as (Shen and Caverly, 2025b)

$$\mathbf{J}_b^{\mathcal{B}c} \dot{\omega}_b^{ba} + \omega_b^{ba \times} \mathbf{J}_b^{\mathcal{B}c} \omega_b^{ba} + \omega_b^{ba \times} \mathbf{h}_b^{\text{RW}} + \dot{\mathbf{h}}_b^{\text{RW}} + \frac{m_p^3 + m_s^3}{(m_p + m_s)^2} \left(\mathbf{r}_b^{ps \times} \ddot{\mathbf{r}}_b^{ps} - 2 \dot{\mathbf{r}}_b^{ps \times} \mathbf{r}_b^{ps} \omega_b^{ba} \right) = \boldsymbol{\tau}_b^{\mathcal{B}c}, \quad (1)$$

where ω_b^{ba} is the angular velocity of \mathcal{F}_b relative to \mathcal{F}_a resolved in \mathcal{F}_b , \mathbf{h}_b^{RW} is the collective angular momentum of the RWs relative to the CM of the bus (point p) with respect to inertial reference frame \mathcal{F}_a resolved in \mathcal{F}_b . The term $\boldsymbol{\tau}_b^{\mathcal{B}c} = \boldsymbol{\tau}_b^{\text{AMT}} + \boldsymbol{\tau}_b^{\text{RCD}} + \boldsymbol{\tau}_b^{\text{dist}}$ is the torque acting on the sailcraft relative to its CM, consisting of the AMT-SRP-induced torque $\boldsymbol{\tau}_b^{\text{AMT}} = \frac{m_s}{m_p + m_s} \mathbf{r}_b^{ps \times} \mathbf{f}_b^{\text{SRP}}$, the RCD torque $\boldsymbol{\tau}_b^{\text{RCD}}$, and the disturbance torque $\boldsymbol{\tau}_b^{\text{dist}}$. The term $\mathbf{f}_b^{\text{SRP}}$ denotes the solar radiation pressure induced force acting on the sail's CP. It is assumed that SRP force $\mathbf{f}_b^{\text{SRP}}$ and disturbance torque $\boldsymbol{\tau}_b^{\text{dist}}$ are constant, which is justified given the slow evolution of the sailcraft attitude in this work. The RCD torque is generated by activating one of the set of four RCDs (either brown or orange) visualized in Fig. 1(a). Actuating the orange RCDs generates a positive roll torque about $\overset{\rightarrow}{b^3}$ axis, while actuating the brown RCDs generates a negative torque about this same axis. The time-dependencies of $\mathbf{J}_b^{\mathcal{B}c}(t)$, $\mathbf{r}_b^{ps}(t)$, $\omega_b^{ba}(t)$, $\mathbf{h}_b^{\text{RW}}(t)$, $\boldsymbol{\tau}_b^{\mathcal{B}c}(t)$ are omitted for brevity in Eq. (1).

A 3-2-1 Euler angle sequence is used to describe the rotation between \mathcal{F}_a and \mathcal{F}_b , so that $\mathbf{C}_{ba} = \mathbf{C}_1(\theta_1) \mathbf{C}_2(\theta_2) \mathbf{C}_3(\theta_3)$ is the DCM describing the orientation of \mathcal{F}_b relative to \mathcal{F}_a , where $\mathbf{C}_i(\cdot)$ is the DCM representing a rotation about the i -th principal axis. The mapping $\omega_b^{ba} = \mathbf{S}(\boldsymbol{\theta}) \dot{\boldsymbol{\theta}}$ relates Euler angle rates to angular velocity, where the matrix $\boldsymbol{\theta} = [\theta_1 \ \theta_2 \ \theta_3]^\top$ is the set of Euler angles and $\mathbf{S}(\boldsymbol{\theta})$ is the mapping matrix. It is worth noting that $\mathbf{S}(\boldsymbol{\theta})$ depends only on θ_1 and θ_2 due to the selected 3-2-1 Euler angle sequence. Given that a solar sail is designed to keep the Sun within its field of view and maintain a nominal spin about the $\overset{\rightarrow}{b^3}$ axis, this choice allows for ease of linearization about any nominal angular velocity about the $\overset{\rightarrow}{b^3}$ axis, and positions the kinematic singularity at 180° from the nominal inertial pointing attitude.

2.3. Reaction Wheel Control and Allocation

The RWs onboard the sailcraft generate the vehicle's attitude control torques through an increase or decrease in the angular momentum of the RWs. Solar Cruiser has a 4-RW assembly, which requires control allocation to determine the action to be taken by each individual RW in order to generate the required attitude control torque. Details regarding the attitude control law, the RW geometric configuration, and the RW control allocation methodology used in this work are presented in this section.

2.3.1. Attitude Control Law

Many advanced RW attitude control methods exist that could be implemented to meet the solar sail's attitude control requirements. This paper employs a simple PID attitude control law to mimic the controller developed for Solar Cruiser (Inness et al., 2023). The desired control torque to be generated by the RWs is defined through a PID control law as

$$\boldsymbol{\tau}_{b,\text{des}}^{\text{RW}} = -\dot{\mathbf{h}}_{b,\text{des}}^{\text{RW}} = -\mathbf{K}_p \tilde{\boldsymbol{\theta}}(t) - \mathbf{K}_d \dot{\tilde{\boldsymbol{\theta}}}(t) - \mathbf{K}_i \int_{t_0}^t \tilde{\boldsymbol{\theta}}(\tau) d\tau, \quad (2)$$

where $\tilde{\boldsymbol{\theta}}(t) = \boldsymbol{\theta}(t) - \boldsymbol{\theta}_d$, $\dot{\tilde{\boldsymbol{\theta}}}(t) = \dot{\boldsymbol{\theta}}(t) - \dot{\boldsymbol{\theta}}_d$, and $\boldsymbol{\theta}_d$, $\dot{\boldsymbol{\theta}}_d$ are the desired Euler angles and Euler angle rates of the desired trajectory, respectively. In this work, $\boldsymbol{\theta}_d$ and $\dot{\boldsymbol{\theta}}_d$ are chosen to be $\mathbf{0}$ for simplicity, although this is not a fundamental limitation of the proposed momentum management approach.

2.3.2. Reaction Wheels Assembly Geometry

Solar Cruiser uses four RWs as its primary attitude control actuators (Inness et al., 2023). The attitude dynamics, as established in Eq. (1) within the sailcraft's body frame, include the three-dimensional total angular momentum of

the four RWs, \mathbf{h}_b^{RW} , as well as its time derivative $\dot{\mathbf{h}}_b^{\text{RW}}$. The variables \mathbf{h}_b^{RW} and $\dot{\mathbf{h}}_b^{\text{RW}}$ represent projections of the angular momentum of the 4-RW configuration onto the three body-frame axes. This results in the linear relationships

$$\mathbf{h}_b^{\text{RW}} = \mathbf{M}_{34} \mathbf{h}_4^{\text{RW}},$$

and

$$\dot{\mathbf{h}}_b^{\text{RW}} = \mathbf{M}_{34} \dot{\mathbf{h}}_4^{\text{RW}},$$

where $\mathbf{h}_4^{\text{RW}} = [h_1 \ h_2 \ h_3 \ h_4]^T$ comprises the four individual RW angular momentum values. The allocation matrix $\mathbf{M}_{34} \in \mathbb{R}^{3 \times 4}$ is time invariant and is determined entirely by the geometric configuration of the four RWs. The time-derivative of the total RW angular momentum projected onto the body frame directly yields the reaction torque exerted on the spacecraft, where $\dot{\mathbf{h}}_b^{\text{RW}} = -\boldsymbol{\tau}_b^{\text{RW}}$.

The optimal geometric configuration of a 4-RW assembly has been investigated extensively in the literature (Ismail and Varatharajoo, 2010; Bellar et al., 2016; Lee et al., 2017; Leve et al., 2015; Markley and Crassidis, 2014). In the absence of any direct information regarding the configuration used by Solar Cruiser, the common pyramidal configuration is used, where it is assumed that the spin axis of each RW passes through the CM of the sailcraft bus. This choice of RW configuration only affects the definition of \mathbf{M}_{34} , allowing the methods presented in this paper to be adapted to other configurations if desired.

To derive the expression for \mathbf{M}_{34} , consider the i -th RW as a rigid disk rotating about its axis of symmetry $\overset{\rightarrow}{w_i^3}$, in its rotating frame \mathcal{F}_{w_i} . The reference frame \mathcal{F}_{w_i} is obtained from \mathcal{F}_b by rotating ψ_i about $\overset{\rightarrow}{b^3}$, then rotating ϕ_i about the rotated $\overset{\rightarrow}{b^2}$ axis. In this paper $\psi_i = 60^\circ$ for all i , and $\phi_i = 45^\circ + (i-1) \cdot 90^\circ$, $i = 1, 2, 3, 4$. The DCM defining the orientation of \mathcal{F}_{w_i} relative to the body frame \mathcal{F}_b is given by

$$\mathbf{C}_{w_i b} = \mathbf{C}_{bw_i}^T = \mathbf{C}_2(\phi_i) \mathbf{C}_3(\psi_i) = \begin{bmatrix} \cos \phi_i \cos \psi_i & \cos \phi_i \sin \psi_i & -\sin \phi_i \\ -\sin \psi_i & \cos \psi_i & 0 \\ \sin \phi_i \cos \psi_i & \sin \phi_i \sin \psi_i & \cos \phi_i \end{bmatrix}.$$

The angular velocity of \mathcal{F}_{w_i} relative to \mathcal{F}_b expressed in \mathcal{F}_b is

$$\boldsymbol{\omega}_b^{w_i b} = \mathbf{C}_{bw_i} \begin{bmatrix} 0 \\ 0 \\ \dot{\gamma}_i \end{bmatrix} = \begin{bmatrix} \sin \phi_i \cos \psi_i \\ \sin \phi_i \sin \psi_i \\ \cos \phi_i \end{bmatrix} \dot{\gamma}_i,$$

where $\dot{\gamma}_i$ denotes the spin rate of the i -th RW. The moment of inertia matrix of the i -th RW is given by $\mathbf{J}_{w_i}^{W_i P} = \text{diag}(\frac{m_w r_w^2}{4}, \frac{m_w r_w^2}{4}, \frac{m_w r_w^2}{2})$, where m_w is the mass of the RW and r_w is the radius of RW. The total angular momentum of the four RWs projected into the body frame is obtained by summing the individual contributions, which establishes the final kinematic mapping

$$\begin{aligned} \mathbf{h}_b^{\text{RW}} &= \sum_{i=1}^4 \mathbf{C}_{bw_i} \mathbf{J}_{w_i}^{W_i P} \mathbf{C}_{bw_i}^T \boldsymbol{\omega}_b^{w_i b} \\ &= \sum_{i=1}^4 \mathbf{C}_{bw_i} \begin{bmatrix} \frac{1}{2} & 0 & 0 \\ 0 & \frac{1}{2} & 0 \\ 0 & 0 & 1 \end{bmatrix} \mathbf{C}_{bw_i}^T \begin{bmatrix} \sin \phi_i \cos \psi_i \\ \sin \phi_i \sin \psi_i \\ \cos \phi_i \end{bmatrix} \dot{\gamma}_i \\ &= \mathbf{M}_{34} \mathbf{h}_4^{\text{RW}}, \end{aligned}$$

where $h_i = \frac{1}{2} m_w r_w^2 \dot{\gamma}_i$ is the angular momentum of the i -th RW resolved in frame \mathcal{F}_{w_i} and

$$\mathbf{M}_{34} = \left[\mathbf{C}_{bw_1} \begin{bmatrix} \frac{1}{2} & 0 & 0 \\ 0 & \frac{1}{2} & 0 \\ 0 & 0 & 1 \end{bmatrix} \mathbf{C}_{bw_1}^T \begin{bmatrix} \sin \phi_1 \cos \psi_1 \\ \sin \phi_1 \sin \psi_1 \\ \cos \phi_1 \end{bmatrix} \quad \dots \quad \mathbf{C}_{bw_4} \begin{bmatrix} \frac{1}{2} & 0 & 0 \\ 0 & \frac{1}{2} & 0 \\ 0 & 0 & 1 \end{bmatrix} \mathbf{C}_{bw_4}^T \begin{bmatrix} \sin \phi_4 \cos \psi_4 \\ \sin \phi_4 \sin \psi_4 \\ \cos \phi_4 \end{bmatrix} \right].$$

Substituting in the numerical parameters $\psi_i = 60^\circ$ for all i , and $\phi_i = 45^\circ + (i-1) \cdot 90^\circ$, $i = 1, 2, 3, 4$ results in

$$\mathbf{M}_{34} = \begin{bmatrix} 0.6124 & -0.6124 & -0.6124 & 0.6124 \\ 0.6124 & 0.6124 & -0.6124 & -0.6124 \\ 0.5 & 0.5 & 0.5 & 0.5 \end{bmatrix}. \quad (3)$$

2.3.3. Unconstrained Minimum-Norm Allocation

The PID control law in Eq. (2) determines the desired angular momentum derivative in the body-frame $\dot{\mathbf{h}}_{b,\text{des}}^{\text{RW}}$, which then needs to be allocated to the momentum of the individual RWs within the 4-RW assembly. Since the mapping between \mathbf{h}_b^{RW} and \mathbf{h}_4^{RW} is under-determined (i.e., four variables are to be determined from three equations), the allocation problem is inherently non-unique.

The selection of an optimal allocation is typically a core redundancy and safety design choice within the attitude determination and control system (ADCS). For the purpose of developing momentum management techniques in this paper, a computationally-efficient pseudo-inverse method is employed to define this allocation uniquely, where

$$\mathbf{h}_4^{\text{RW}} = \mathbf{M}_{34}^\dagger \mathbf{h}_{b,\text{des}}^{\text{RW}}, \quad (4)$$

$$\dot{\mathbf{h}}_4^{\text{RW}} = \mathbf{M}_{34}^\dagger \dot{\mathbf{h}}_{b,\text{des}}^{\text{RW}}, \quad (5)$$

and $\mathbf{M}_{34}^\dagger = \mathbf{M}_{34}^T (\mathbf{M}_{34} \mathbf{M}_{34}^T)^{-1}$. This approach yields the minimum-norm pseudo-inverse result for \mathbf{h}_4^{RW} and $\dot{\mathbf{h}}_4^{\text{RW}}$, characterized by the smallest possible Euclidean norm ($\|\mathbf{h}_4^{\text{RW}}\|_2$ and $\|\dot{\mathbf{h}}_4^{\text{RW}}\|_2$) amongst all potential combinations that yield the desired values of $\mathbf{h}_{b,\text{des}}^{\text{RW}}$ and $\dot{\mathbf{h}}_{b,\text{des}}^{\text{RW}}$. In the absence of any RW saturation, Eq. (5) is used to compute $\dot{\mathbf{h}}_4^{\text{RW}}$.

2.3.4. Constrained Minimum-Norm Allocation via Sequential Pseudo-Inverse

The standard pseudo-inverse solution from Eq. (4) may generate wheel momentum commands that exceed the physical saturation limit of one or more RWs (i.e., $\|\mathbf{h}_4^{\text{RW}}\|_\infty > h_{\max}^{\text{RW}}$, where h_{\max}^{RW} is the saturation limit). A constraint-prioritized sequential allocation scheme is applied to manage the inherent redundancy while rigorously enforcing these physical saturation constraints. This scheme is designed to find a solution to the minimization of $\|\mathbf{h}_4^{\text{RW}}\|_2$ subject to the constraint $\|\mathbf{h}_4^{\text{RW}}\|_\infty \leq h_{\max}^{\text{RW}}$ in a computationally-efficient manner. Although this could be posed as a QP, the relatively short time steps associated with attitude control necessitates a more computationally-efficient strategy. To meet this need, a suboptimal solution is found through the proposed method that operates by sequentially checking the maximum individual RW angular momentum, enforcing saturation limit, and redistributing angular momentum on unsaturated RWs to satisfy the desired RW attitude control torque. The process is as follows:

- 1. Unconstrained Initial Solution and Saturation Check:** The process commences by calculating the unconstrained minimum-norm solution using the current body-frame angular momentum $\mathbf{h}_4^{\text{RW}} = \mathbf{M}_{34}^\dagger \mathbf{h}_{b,\text{des}}^{\text{RW}}$. The resulting unconstrained 4-RW momentum is checked against the saturation limit, where $\|\mathbf{h}_4^{\text{RW}}\|_\infty \leq h_{\max}^{\text{RW}}$ must be satisfied. If $\|\mathbf{h}_4^{\text{RW}}\|_\infty \leq h_{\max}^{\text{RW}}$ is satisfied (none of the RWs saturate), the mapping of the angular momentum derivative is $\dot{\mathbf{h}}_4^{\text{RW}} = \mathbf{M}_{34}^\dagger \dot{\mathbf{h}}_{b,\text{des}}^{\text{RW}}$, the constrained minimum-norm allocation is determined, and the remaining steps can be skipped. If $\|\mathbf{h}_4^{\text{RW}}\|_\infty > h_{\max}^{\text{RW}}$ (at least one of the RWs saturate), the process continues to Steps 2 through 4.
- 2. Saturation Implementation:** The component of \mathbf{h}_4^{RW} with the largest magnitude exceeding the saturation limit h_{\max}^{RW} is identified. This is labeled as the i -th component of \mathbf{h}_4^{RW} (i.e., $h_4^{\text{RW},(i)}$), where $|h_4^{\text{RW},(i)}| = \|\mathbf{h}_4^{\text{RW}}\|_\infty$ and $|h_4^{\text{RW},(i)}| > h_{\max}^{\text{RW}}$. The i -th RW is now identified as saturated for all remaining iterations. Then, its momentum is fixed at the saturation boundary $h_{4,\text{sat}}^{\text{RW},(i)} = \pm h_{\max}^{\text{RW}}$, where the sign of the momentum $h_4^{\text{RW},(i)}$ is maintained. Crucially, when a wheel's angular momentum is saturated and fixed, its corresponding commanded angular momentum derivative $\dot{h}_4^{\text{RW},(i)}$ must simultaneously be set to zero to prevent the controller from commanding further change into the limit, i.e., $\dot{h}_{4,\text{sat}}^{\text{RW},(i)} = 0$.
- 3. Residual Calculation and Redistribution:** The momentum contribution from the saturated wheel(s) is calculated and subtracted from the original demanded body-frame angular momentum. This yields the residual momentum requirement for the remaining unsaturated wheels

$$\mathbf{h}_b^{\text{res}} = \mathbf{h}_{b,\text{des}}^{\text{RW}} - \mathbf{M}_{34}^{\text{sat}} \mathbf{h}_{4,\text{sat}}^{\text{RW}},$$

where $\mathbf{M}_{34}^{\text{sat}}$ is a modified version of the allocation matrix, where the columns corresponding to the unsaturated wheels are set to zero and $\mathbf{h}_{4,\text{sat}}^{\text{RW}} \in \mathbb{R}^4$ contains $\pm h_{\max}^{\text{RW}}$ in the entries associated with saturated wheels and zeros in the other entries of the matrix.

The angular momentum of the n unsaturated wheels is then recalculated as

$$\mathbf{h}_{n,\text{unsat}}^{\text{RW}} = (\mathbf{M}_{3 \times n}^{\text{unsat}})^\dagger \mathbf{h}_b^{\text{res}}, \quad (6)$$

where $\mathbf{M}_{3 \times n}^{\text{unsat}}$ is a modified version of the allocation matrix \mathbf{M}_{34} such that the columns associated with the saturated wheels are removed, reducing its dimension to $3 \times n$. The allocation of the unsaturated wheels angular momentum rate is computed similarly as

$$\dot{\mathbf{h}}_{n,\text{unsat}}^{\text{RW}} = (\mathbf{M}_{3 \times n}^{\text{unsat}})^{\dagger} \dot{\mathbf{h}}_{b,\text{des}}^{\text{RW}}. \quad (7)$$

4. **Saturation Assessment:** The results of Steps 2 and 3 are compiled to obtain updated values of \mathbf{h}_4^{RW} and $\dot{\mathbf{h}}_4^{\text{RW}}$. The entries of \mathbf{h}_4^{RW} associated with saturated wheels are set using the appropriate entries of $\mathbf{h}_{4,\text{sat}}^{\text{RW}}$, while the unsaturated wheel values are found using the result from Eq. (6). The entries of $\dot{\mathbf{h}}_4^{\text{RW}}$ associated with saturated wheels are set to zero, while the unsaturated wheel values are chosen using Eq. (7).

If $\|\mathbf{h}_4^{\text{RW}}\|_{\infty} \leq h_{\max}^{\text{RW}}$, then the allocation process is completed. Else, the process returns to Step 2.

Steps 2 through 4 of this process continue recursively until all components of the final wheel momentum \mathbf{h}_4^{RW} are within $\pm h_{\max}^{\text{RW}}$. Note that the initial pseudo-inverse solved in Step 1 determines an allocation with the smallest magnitude for the under-determined systems. When 1 RW saturates ($n = 3$), the reduced mapping becomes an one-to-one inverse mapping, leading to a unique solution in the allocation of the unsaturated wheels. When 2 or 3 RWs are identified as saturated ($n \in \{1, 2\}$), the mapping becomes an over-determined system, and an exact solution does not exist. In this case, the allocations performed in Eqs. (6) and (7) of Step 3 become a least-squares problems. A direct consequence of this is that the rate of change of the angular momentum in the 4 RWs, $\dot{\mathbf{h}}_4^{\text{RW}}$, will not necessarily produce the desired value of $\dot{\mathbf{h}}_{b,\text{des}}^{\text{RW}}$ from the attitude control in Eq. (2), and performance of the attitude controller may suffer. When all RWs saturate, the 4-RW system can no longer provide any torque and attitude control is no longer possible.

2.4. Momentum Management Control Actuation

The momentum management time step is chosen based on the AMT position command update period of $\Delta t = 100$ seconds used on NEA Scout (Orphee et al., 2018), which is much longer than the attitude control (or ADCS) time step that is assumed to be one second in this work. Between momentum management time steps, the AMT and RCD inputs are modeled with zeroth-order-hold (ZOH) discretization. This ZOH is also used when implementing the momentum management and attitude control inputs within the continuous-time numerical simulation of the sailcraft's nonlinear dynamics.

The AMT actuation input \mathbf{u}^{AMT} is associated with the first two components of \mathbf{r}_b^{ps} , where $\mathbf{u}^{\text{AMT}} = [r_{b1}^{\text{AMT}} \quad r_{b2}^{\text{AMT}}]^T$. The layout of Solar Cruiser's RCDs allows for an approximately pure on-off roll momentum management torque to be generated in either direction (Inness et al., 2023; Tyler et al., 2023; Heaton et al., 2023). Thus, the RCD torque is modeled as $\tau_b^{\text{RCD}} = [0 \quad 0 \quad \tau_{b3}^{\text{RCD}}]^T$, where $\tau^{\text{RCD}} = \tau_{b3}^{\text{RCD}}$ is chosen based on the momentum management strategy. Considering the RCD on-off actuation as an explicit constraint in the MPC optimization problem leads to a mixed-integer problem, which is computationally expensive, and limits the practicality of onboard real-time MPC. To enable the use of convex optimization solvers with the proposed MPC policy, the integer constraint is relaxed, and a PWM quantization is applied to the RCD actuation (Shen and Caverly, 2025b). A continuous value of $u_{\text{mpc}}^{\text{RCD}}$ is allowed in the optimization problem, where $-\tau_{b3,\text{on}}^{\text{RCD}} \leq u_{\text{mpc}}^{\text{RCD}} \leq \tau_{b3,\text{on}}^{\text{RCD}}$ and $\tau_{b3,\text{on}}^{\text{RCD}}$ is the roll torque magnitude generated when the RCDs are turned on. After solving the MPC optimization problem, the continuous $u_{\text{mpc}}^{\text{RCD}}$ is then quantized into a discrete value

$$u^{\text{RCD}}(t) = \begin{cases} \beta_{\text{on}} \tau_{b3,\text{on}}^{\text{RCD}}, & \text{for } t_k \leq t < (t_k + t_c), \\ 0, & \text{for } (t_k + t_c) \leq t < t_{k+1}, \end{cases} \quad (8)$$

where $\beta_{\text{on}} \in \{-1, 1\}$ denotes the clockwise and counterclockwise directions about the roll (b^3) axis, $\tau_{b3,\text{on}}^{\text{RCD}}$ denotes the torque magnitude when RCDs are turned on, and $t_c = \Delta t \cdot \frac{u_{\text{mpc}}^{\text{RCD}}}{\tau_{b3,\text{on}}^{\text{RCD}}}$ is the length (cut-off time) of a single pulse PWM conversion from a continuous MPC optimal RCD input. In general, $\tau_{b3,\text{on}}^{\text{RCD}}$ depends on the sun incidence angle (SIA), however, a constant SIA, and thus a constant value of $\tau_{b3,\text{on}}^{\text{RCD}}$, is considered in this study. Details of the RCD quantization can be found in the work of Shen and Caverly (2025b).

2.5. Linear Dynamic Model for Estimation and Prediction

For practical onboard implementation, a linear model is required for disturbance estimation and predictive control. The accuracy of the model significantly affects the performance of the controller. However, higher model fidelity comes

at the cost of increased computational demand. To enable real-time onboard implementation, a trade-off must be made between prediction accuracy and computational feasibility. Although a nonlinear dynamics model would have higher fidelity, it is not practical to consider the implementation of nonlinear MPC onboard with current technology due to their excessive computation demand. A discrete-time linear model is thus used to supplement onboard disturbance estimation and predictive control, specifically the process model in Kalman filter and the prediction model in MPC.

The nonlinear dynamic model is linearized about the current state and AMT position at every time step. Since future AMT positions and RCD torques are not known in advance, their rates are assumed to be zero in the linearization. This yields a continuous-time linear time-varying (LTV) model, where the states include the attitude, angular velocity, reaction wheel angular momentum, and an integral state from the integral term of the attitude controller. The state of the linear system is denoted as $\mathbf{x} = [\boldsymbol{\theta}^\top \ \omega_b^{ba^\top} \ \mathbf{h}_b^{\text{RW}^\top} \ \mathbf{e}^{\text{int}^\top}]^\top$, where $\mathbf{e}^{\text{int}} = \int_{t_0}^t (\boldsymbol{\theta}(\tau) - \boldsymbol{\theta}_d) d\tau$ is the internal state representing the integral term of PID law. It is assumed that the SRP force is constant, and perfectly known from the onboard ADCS. External disturbances are represented by $\mathbf{w} = \boldsymbol{\tau}_b^{\text{dist}}$, while \mathbf{u}^{AMT} and u^{RCD} denote the AMT position and RCD torque input, respectively. The linearized continuous-time dynamics retaining the first-order term of Taylor series expansion is derived as (Shen and Caverly, 2025b)

$$\dot{\mathbf{x}} = \mathbf{A}\mathbf{x} + \mathbf{B}_w\mathbf{w} + \mathbf{B}_{u1}\mathbf{u}^{\text{AMT}} + \mathbf{B}_{u2}u^{\text{RCD}}, \quad (9)$$

where

$$\mathbf{A} = \mathbf{A}(\bar{\mathbf{x}}, \bar{\mathbf{r}}_b^{ps}) = \begin{bmatrix} \mathbf{0}_{3 \times 3} & \mathbf{1}_{3 \times 3} & \mathbf{0}_{3 \times 3} & \mathbf{0}_{3 \times 3} \\ -\bar{\mathbf{J}}_b^{\mathcal{B}c^{-1}} \mathbf{K}_p & \frac{\partial \mathbf{f}_2}{\partial \omega_b^{ba}} \Big|_{\bar{\mathbf{x}}, \bar{\mathbf{u}}} & -\bar{\mathbf{J}}_b^{\mathcal{B}c^{-1}} \bar{\omega}_b^{ba^\times} & -\bar{\mathbf{J}}_b^{\mathcal{B}c^{-1}} \mathbf{K}_i \\ \mathbf{K}_p & \mathbf{K}_d & \mathbf{0}_{3 \times 3} & \mathbf{K}_i \\ \mathbf{1}_{3 \times 3} & \mathbf{0}_{3 \times 3} & \mathbf{0}_{3 \times 3} & \mathbf{0}_{3 \times 3} \end{bmatrix},$$

$$\mathbf{B}_w = \mathbf{B}_w(\bar{\mathbf{r}}_b^{ps}) = \begin{bmatrix} \mathbf{0}_{3 \times 3} \\ \bar{\mathbf{J}}_b^{\mathcal{B}c^{-1}} \\ \mathbf{0}_{3 \times 3} \\ \mathbf{0}_{3 \times 3} \end{bmatrix}, \quad \mathbf{B}_{u1} = \mathbf{B}_{u1}(\bar{\mathbf{x}}, \bar{\mathbf{r}}_b^{ps}) = \begin{bmatrix} \mathbf{0}_{3 \times 2} \\ \frac{\partial \mathbf{f}_2}{\partial \mathbf{r}_b^{ps}} \Big|_{\bar{\mathbf{x}}, \bar{\mathbf{u}}} \begin{bmatrix} \mathbf{1}_{2 \times 2} \\ \mathbf{0}_{1 \times 2} \end{bmatrix} \\ \mathbf{0}_{3 \times 2} \\ \mathbf{0}_{3 \times 2} \end{bmatrix}, \quad \mathbf{B}_{u2} = \mathbf{B}_{u2}(\bar{\mathbf{r}}_b^{ps}) = \begin{bmatrix} \mathbf{0}_{3 \times 3} \\ \bar{\mathbf{J}}_b^{\mathcal{B}c^{-1}} \\ \mathbf{0}_{3 \times 3} \\ \mathbf{0}_{3 \times 3} \end{bmatrix} \begin{bmatrix} 0 \\ 0 \\ 1 \end{bmatrix},$$

and

$$\frac{\partial \mathbf{f}_2}{\partial \omega_b^{ba}} \Big|_{\bar{\mathbf{x}}, \bar{\mathbf{r}}_b^{ps}} = \bar{\mathbf{J}}_b^{\mathcal{B}c^{-1}} \left((\bar{\mathbf{J}}_b^{\mathcal{B}c} \bar{\omega}_b^{ba})^\times - \bar{\omega}_b^{ba^\times} \bar{\mathbf{J}}_b^{\mathcal{B}c} + \bar{\mathbf{h}}_b^{\text{RW}^\times} - \mathbf{K}_d \right),$$

$$\frac{\partial \mathbf{f}_2}{\partial \mathbf{r}_b^{ps}} \Big|_{\bar{\mathbf{x}}, \bar{\mathbf{r}}_b^{ps}} = \bar{\mathbf{J}}_b^{\mathcal{B}c^{-1}} \left(-\frac{m_p^3 + m_s^3}{(m_p + m_s)^2} \bar{\omega}_b^{ba^\times} (\bar{\mathbf{r}}_b^{ps^\times} \bar{\omega}_b^{ba^\times} + (\bar{\mathbf{r}}_b^{ps^\times} \bar{\omega}_b^{ba})^\times) - \frac{m_p^3 + m_s^3}{(m_p + m_s)^2} (\bar{\mathbf{r}}_b^{ps^\times} \dot{\bar{\omega}}_b^{ba^\times} + (\bar{\mathbf{r}}_b^{ps^\times} \dot{\bar{\omega}}_b^{ba})^\times) - \frac{m_s}{m_p + m_s} \mathbf{f}_b^{\text{SRP}^\times} \right).$$

Note that the state-space matrices depend on $\bar{\mathbf{r}}_b^{ps}$ because $\bar{\mathbf{J}}_b^{\mathcal{B}c}$ is a function of \mathbf{r}_b^{ps} . The variables $\bar{\mathbf{x}} = [\bar{\boldsymbol{\theta}}^\top \ \bar{\omega}_b^{ba^\top} \ \bar{\mathbf{h}}_b^{\text{RW}^\top} \ \bar{\mathbf{e}}^{\text{int}^\top}]^\top$ and $\bar{\mathbf{r}}_b^{ps}$ represents the current system state and AMT position, respectively, which are chosen as the current values when performing the linearization.

In this work, a ZOH discretization on both AMT and RCD actuation is used, which has a lower computation requirement when compared to the mixed-FOH-ZOH discretization employed by Shen and Caverly (2025a). Compared to a FOH-discretized model, the ZOH-discretization model does not require numerical integration at every momentum management time step. Discretizing Eq. (9) using a ZOH with the momentum management timestep Δt results in

$$\mathbf{x}_k = \mathbf{A}_k \mathbf{x}_k + \mathbf{B}_{w,k} \mathbf{w}_k + \mathbf{B}_{u1,k} \mathbf{u}_k^{\text{AMT}} + \mathbf{B}_{u2,k} u_k^{\text{RCD}}, \quad (10)$$

which is used as the the Kalman filter process model and MPC prediction model. Note that the nonlinear dynamics in Eq. (1) are used as the system's dynamics for all numerical simulations, while the KF and MPC use the discrete-time LTV model. Section 3 presents a state and disturbance estimation framework based on a Kalman filter that is used to yield the estimates $\hat{\mathbf{x}}(t_k)$ and $\hat{\mathbf{w}}(t_k)$ needed to compute the LTV dynamic model used in MPC.

3. Disturbance Estimation Using Kalman Filter

The disturbance torque $\boldsymbol{\tau}_b^{\text{dist}}$ is an external input acting on the solar sail system that impacts its dynamics. In the MPC policy proposed in Section 4, this disturbance torque is a key parameter in the prediction model used to

forecast the system dynamics and determine optimal momentum management actuation. Due to the slow motion and relatively steady attitude operation nature of solar sails, the disturbance torque is modeled as approximately constant or slow varying. However, the disturbance cannot be measured directly, and needs to be estimated onboard. Utilizing a Kalman filter estimation framework provides adequate knowledge of the disturbance that MPC can take advantage of. A Kalman filter framework is developed in this section to supplement this essential parameter for MPC.

3.1. Measurement Model

Solar Cruiser's ADCS provides an accurate estimate of the sailcraft's attitude, angular velocity, and angular momentum using onboard sensors such as rate gyros, inertial measurement units (IMUs), sun sensors, and star trackers. It is thus assumed in this work that a full state measurement of $\mathbf{x}_k = [\theta_k^T \ \omega_{b,k}^{ba^T} \ \mathbf{h}_{b,k}^{RW^T} \ \mathbf{e}_k^{int^T}]^T$ is accessible, and the measurement noise is normally distributed, resulting in the measurement model

$$\mathbf{z}_{1,k} = \underbrace{[\mathbf{1}_{12 \times 12} \ \mathbf{0}_{12 \times 3}]}_{\mathbf{H}_1} \begin{bmatrix} \mathbf{x}_k \\ \mathbf{w}_k \end{bmatrix} + \mathbf{v}_{1,k}, \quad \mathbf{v}_{1,k} \sim \mathcal{N}(\mathbf{0}, \mathbf{R}_1^{KF}),$$

where $\mathbf{v}_{1,k}$ is the linear additive measurement noise, and the measurement error covariance matrix $\mathbf{R}_1^{KF} = \text{diag}(\mathbf{r}_\theta, \mathbf{r}_\omega, \mathbf{r}_h, \mathbf{r}_e)$ is determined by the variance of each corresponding state measurement error ($\sigma_\theta^2, \sigma_\omega^2, \sigma_h^2, \sigma_e^2$), which is associated with the onboard ADCS state estimation accuracy. Considering that the RW PID control law dictates the reaction wheel angular momentum rate $\dot{\mathbf{h}}_{b,k}^{RW^T}$, an additional measurement of $\dot{\mathbf{h}}_{b,k}^{RW^T}$ is assumed to be accessible to improve observability, where

$$\mathbf{z}_{2,k} = \underbrace{[\mathbf{K}_p \ \mathbf{K}_d \ \mathbf{0}_{3 \times 3} \ \mathbf{K}_i \ \mathbf{0}_{3 \times 3}]}_{\mathbf{H}_2} \begin{bmatrix} \mathbf{x}_k \\ \mathbf{w}_k \end{bmatrix} + \mathbf{v}_{2,k}, \quad \mathbf{v}_{2,k} \sim \mathcal{N}(\mathbf{0}, \mathbf{R}_2^{KF}),$$

$\mathbf{v}_{2,k}$ is the linear additive measurement noise, and the measurement error covariance matrix $\mathbf{R}_2^{KF} = \mathbf{r}_h$ is associated to the variance of each corresponding state measurement error in \mathbf{R}_1^{KF} .

The complete Kalman measurement model is formulated as

$$\underbrace{\begin{bmatrix} \mathbf{z}_{1,k} \\ \mathbf{z}_{2,k} \end{bmatrix}}_{\mathbf{z}_k} = \underbrace{\begin{bmatrix} \mathbf{H}_1 \\ \mathbf{H}_2 \end{bmatrix}}_{\mathbf{H}} \begin{bmatrix} \mathbf{x}_k \\ \mathbf{w}_k \end{bmatrix} + \underbrace{\begin{bmatrix} \mathbf{v}_{1,k} \\ \mathbf{v}_{2,k} \end{bmatrix}}_{\mathbf{v}_k}, \quad \mathbf{v}_k \sim \mathcal{N}(\mathbf{0}, \mathbf{R}^{KF}),$$

where $\mathbf{R}^{KF} = \text{diag}(\mathbf{r}_\theta, \mathbf{r}_\omega, \mathbf{r}_h, \mathbf{r}_e, \mathbf{r}_h)$.

3.2. Process Model

Given the slow evolution of the spacecraft attitude, it is assumed that SRP force $\mathbf{f}_b^{\text{SRP}}$ is a known constant, the error of the dynamic model is Gaussian and linearly additive, and the disturbance torque to be estimated, τ_b^{dist} , is constant. The discrete-time LTV model in Eq. (10) with the addition of linear model error is given by

$$\begin{aligned} \mathbf{x}_{k+1}^{KF} &= \mathbf{A}_k \mathbf{x}_k^{KF} + \mathbf{B}_{w,k} \mathbf{w}_k^{KF} + \mathbf{B}_{u1,k} \mathbf{u}_k^{\text{AMT}} + \mathbf{B}_{u2,k} \mathbf{u}_k^{\text{RCD}} + \boldsymbol{\eta}_k^{\text{model}}, \quad \boldsymbol{\eta}_k^{\text{model}} \sim \mathcal{N}(\mathbf{0}, \mathbf{Q}_{\text{model}}^{KF}), \\ \mathbf{w}_{k+1}^{KF} &= \mathbf{w}_k^{KF} + \boldsymbol{\eta}_k^{\text{dist}}, \quad \boldsymbol{\eta}_k^{\text{dist}} \sim \mathcal{N}(\mathbf{0}, \mathbf{Q}_{\text{dist}}^{KF}), \end{aligned}$$

where the linear model error $\boldsymbol{\eta}_k^{\text{model}}$ and disturbance error $\boldsymbol{\eta}_k^{\text{dist}}$ are assumed to be linearly additive and normally distributed. The error covariance matrices of the model uncertainty are $\mathbf{Q}_{\text{model}}^{KF} = \text{diag}(\mathbf{q}_\theta, \mathbf{q}_\omega, \mathbf{q}_h, \mathbf{q}_e)$ and $\mathbf{Q}_{\text{dist}}^{KF} = \text{diag}(q_{\tau 1}, q_{\tau 2}, q_{\tau 3})$, which are tuning parameters chosen to influence the Kalman filter's aggressiveness in updating the estimate of the disturbance torque \mathbf{w}^{KF} . In particular, increasing the variances within $\mathbf{Q}_{\text{model}}^{KF}$ results in a slower convergence of the disturbance torque, while increase the variances within $\mathbf{Q}_{\text{dist}}^{KF}$ speeds up the convergence, while potentially making the estimates more sensitive to measurement noise.

The complete Kalman filter process model is reformulated as

$$\underbrace{\begin{bmatrix} \hat{\mathbf{x}}_{k+1}^- \\ \hat{\mathbf{w}}_{k+1}^- \end{bmatrix}}_{\hat{\mathbf{x}}_{k+1}^-} = \underbrace{\begin{bmatrix} \mathbf{A}_k & \mathbf{B}_{w,k} \\ \mathbf{0}_{3 \times 12} & \mathbf{1}_{3 \times 3} \end{bmatrix}}_{\mathbf{F}_k} \begin{bmatrix} \hat{\mathbf{x}}_k^+ \\ \hat{\mathbf{w}}_k^+ \end{bmatrix} + \underbrace{\begin{bmatrix} \mathbf{B}_{u,k} \\ \mathbf{0}_{3 \times 3} \end{bmatrix}}_{\mathbf{G}_k} \begin{bmatrix} \mathbf{u}_k^{\text{AMT}} \\ \mathbf{u}_k^{\text{RCD}} \end{bmatrix} + \underbrace{\begin{bmatrix} \boldsymbol{\eta}_k^{\text{model}} \\ \boldsymbol{\eta}_k^{\text{dist}} \end{bmatrix}}_{\boldsymbol{\eta}_k},$$

where the process noise is given by $\boldsymbol{\eta}_k \sim \mathcal{N}(\mathbf{0}, \mathbf{Q}^{KF})$ and $\mathbf{Q}^{KF} = \text{diag}(\mathbf{Q}_{\text{model}}^{KF}, \mathbf{Q}_{\text{dist}}^{KF})$.

3.3. Summary of Kalman Filter Estimation Framework

In the time update (prediction) step, the a priori (predicted) state estimate and error covariance are given by

$$\begin{aligned}\hat{\mathbf{X}}_k^- &= \mathbf{F}_{k-1} \hat{\mathbf{X}}_{k-1}^+ + \mathbf{G}_{k-1} \mathbf{U}_{k-1}, \\ \mathbf{P}_k^- &= \mathbf{F}_{k-1} \mathbf{P}_{k-1}^+ \mathbf{F}_{k-1}^\top + \mathbf{Q}^{\text{KF}}.\end{aligned}$$

In the measurement update (correction) step, the a posteriori (updated) state estimate and error covariance are given by

$$\begin{aligned}\hat{\mathbf{X}}_k^+ &= \hat{\mathbf{X}}_k^- + \mathbf{K}_k (\mathbf{Z}_k - \mathbf{H} \hat{\mathbf{X}}_k^-), \\ \mathbf{P}_k^+ &= (\mathbf{I} - \mathbf{K}_k \mathbf{H}) \mathbf{P}_k^-,\end{aligned}$$

where the Kalman gain is computed as $\mathbf{K}_k = \mathbf{P}_k^- \mathbf{H}^\top (\mathbf{H} \mathbf{P}_k^- \mathbf{H}^\top + \mathbf{R}^{\text{KF}})^{-1}$. The state estimate $\hat{\mathbf{X}}_k^+ = [\hat{\mathbf{x}}_k^{+\top} \quad \hat{\mathbf{w}}_k^{+\top}]^\top$ is used within the momentum management controller presented in the following section.

4. Momentum Management Using MPC

Solar sail slew maneuvers are inherently slow due to the small magnitude of SRP torques and the sailcraft's large moment of inertia. As a result, the system dynamics are relatively smooth and predictable, and external disturbances such as SRP imbalance or environmental torques evolve gradually. Moreover, the long time scales involved in solar sail maneuvers provide sufficient computational time for onboard optimization. These characteristics make MPC particularly suitable for solar sail momentum management, where coordinated use of RWs and momentum management actuators (AMT and RCDs) is required to prevent RW saturation while maintaining accurate attitude control. This section presents the MPC framework tailored for solar sail momentum management, specifically designed for Solar Cruiser's configuration.

4.1. Introduction to MPC

MPC is an advanced optimal control strategy that computes control actions by solving a constrained optimization problem over a finite prediction horizon at each time step. It determines a sequence of control inputs that minimize a specified objective function while satisfying the system dynamics, actuator limits, and state constraints. At each control update, MPC uses the current system state and a predictive model to forecast future behavior over a finite horizon of N time steps. It then solves for the optimal sequence of control inputs, yet only the first input is applied to the system. At the next time step, the process is repeated using updated measurements and system information. This receding-horizon strategy enables continual adaptation to disturbances and modeling inaccuracies, providing robust feedback control in the presence of uncertainty.

Real-time implementation of MPC onboard a flight computer can be realistically achieved by formulating the optimization problem as a convex QP with a quadratic objective function and affine constraints. The use of a linear dynamic prediction model within the MPC framework is required in order for it to be formulated as a QP.

4.2. Prediction Model

In contrast to the state \mathbf{x} used in Section 2.5, a modified state $\mathbf{x}^{\text{MPC}} = [\boldsymbol{\theta}^\top \quad \boldsymbol{\omega}_b^{ba\top} \quad \mathbf{h}_4^{\text{RW}\top} \quad \mathbf{e}^{\text{int}\top}]^\top$ is employed in this MPC framework, where $\mathbf{h}_4^{\text{RW}} = \mathbf{M}_{34}^\dagger \mathbf{h}_b^{\text{RW}}$ follows the pseudo-inverse relationship discussed in Section 2.3. This modification allows for a direct constraint on the angular momentum of the individual RWs within the MPC framework. Although a simple pseudo-inverse mapping is used in this prediction model, the proposed MPC approach is not limited to this specific optimal allocation method. More advanced RW angular momentum allocation synthesis can be used based on the design of the ADCS.

The linearized dynamics in Eq. (9) are modified to obtain a linear prediction model to be used in the MPC framework. Specifically, the linear transformation $\mathbf{x} = \mathbf{T} \mathbf{x}^{\text{MPC}}$ is applied, where $\mathbf{T} = \text{diag}(\mathbf{1}, \mathbf{1}, \mathbf{M}_{34}, \mathbf{1})$ is formed using the RW geometry matrix \mathbf{M}_{34} . The inverse linear transformation $\mathbf{x}^{\text{MPC}} = \mathbf{T}^\dagger \mathbf{x}$ is computed using the pseudo-inverse of \mathbf{M}_{34} as $\mathbf{T}^\dagger = \text{diag}(\mathbf{1}, \mathbf{1}, \mathbf{M}_{34}^\dagger, \mathbf{1})$. Applying these transformations to Eq. (9) yields the linear dynamics

$$\dot{\mathbf{x}}^{\text{MPC}} = \mathbf{A}^{\text{MPC}} \mathbf{x}^{\text{MPC}} + \mathbf{B}_w^{\text{MPC}} \mathbf{w} + \mathbf{B}_{u1}^{\text{MPC}} \mathbf{u}^{\text{AMT}} + \mathbf{B}_{u2}^{\text{MPC}} \mathbf{u}^{\text{RCD}}, \quad (11)$$

where $\mathbf{A}^{\text{MPC}} = \mathbf{T}^\dagger \mathbf{A} \mathbf{T}$, $\mathbf{B}_w^{\text{MPC}} = \mathbf{T}^\dagger \mathbf{B}_w$, $\mathbf{B}_{u1}^{\text{MPC}} = \mathbf{T}^\dagger \mathbf{B}_{u1}$, and $\mathbf{B}_{u2}^{\text{MPC}} = \mathbf{T}^\dagger \mathbf{B}_{u2}$. A ZOH is then applied to the inputs of Eq. (11) to yield the discrete-time linear prediction used by MPC over its prediction model, given by

$$\mathbf{x}_{j+1|t_k}^{\text{MPC}} = \mathbf{A}_k^{\text{MPC}} \mathbf{x}_{j|t_k}^{\text{MPC}} + \mathbf{B}_{w,k}^{\text{MPC}} \mathbf{w}_{j|t_k} + \mathbf{B}_{u1,k}^{\text{MPC}} \mathbf{u}_{j|t_k}^{\text{AMT}} + \mathbf{B}_{u2,k}^{\text{MPC}} \mathbf{u}_{j|t_k}^{\text{RCD}}, \quad j = 0, 1, \dots, N-1, \quad (12)$$

where the subscript $j|t_k$ refers to the j -th discrete time step within the MPC prediction horizon at time step t_k . The LTV matrices of $\mathbf{A}_k^{\text{MPC}}$, $\mathbf{B}_{w,k}^{\text{MPC}}$, $\mathbf{B}_{u1,k}^{\text{MPC}}$, $\mathbf{B}_{u2,k}^{\text{MPC}}$ are updated at every momentum management timestep at time t_k , and kept constant throughout the MPC prediction horizon, resulting in a linear time-invariant (LTI) model over the span of the prediction horizon. The MPC framework uses the state estimate from Kalman filter framework presented in Section 3 as its knowledge within the prediction model, where $\mathbf{x}_{0|t_k}^{\text{MPC}} = [\hat{\theta}_k^\top \quad \hat{\omega}_{b,k}^{ba\top} \quad \mathbf{M}_{34}^\dagger \hat{\mathbf{h}}_{b,k}^{\text{RW}\top} \quad \hat{\mathbf{e}}_k^{\text{int}\top}]^\top$ and $\mathbf{w}_{j|t_k} = \hat{\mathbf{w}}_k^+$, $j = 0, 1, \dots, N-1$.

4.3. State Constraints

To ensure the practical feasibility of the controller, inequality constraints are imposed on the system states. These constraints enforce bounded deviations in sailcraft attitude, angular velocity, RW angular momentum, and integrated attitude error across the prediction horizon as $\theta_{\min} \leq \theta_{j|t_k} \leq \theta_{\max}$, $\omega_{b,\min}^{ba} \leq \omega_{b,j|t_k}^{ba} \leq \omega_{b,\max}^{ba}$, $\mathbf{h}_{4,\min}^{\text{RW}} \leq \mathbf{h}_{4,j|t_k}^{\text{RW}} \leq \mathbf{h}_{4,\max}^{\text{RW}}$, and $\mathbf{e}_{\min}^{\text{int}} \leq \mathbf{e}_{j|t_k}^{\text{int}} \leq \mathbf{e}_{\max}^{\text{int}}$, respectively. Collectively, this is written as the constraint $\mathbf{x}_{\min}^{\text{MPC}} \leq \mathbf{x}_{j|t_k}^{\text{MPC}} \leq \mathbf{x}_{\max}^{\text{MPC}}$.

To further avoid the RW angular momentum approaching the hardware physical saturation limits during sustained disturbance rejection accommodate modeling errors, soft constraints are introduced to incentivize the RW angular momentum to stay within a safe operational margin. These soft bounds are defined as

$$\mathbf{h}_{4,\min}^{\text{soft}} - \alpha \leq \mathbf{h}_{4,j|t_k}^{\text{RW}} \leq \mathbf{h}_{4,\max}^{\text{soft}} + \alpha,$$

where $\mathbf{h}_{4,\min}^{\text{soft}}$ and $\mathbf{h}_{4,\max}^{\text{soft}}$ represent the lower and upper bounds of the soft constraint envelope (i.e., the desired safe operation region), and the non-negative slack variable $\alpha \geq 0$ is quadratically penalized in the MPC objective function, enabling graceful constraint relaxation while encouraging the system to remain within the nominal safe range. Within the soft bounds, the slack variable remains zero and no penalty is incurred. When violated, the controller attempts to reduce the non-zero value of α to drive the RWs angular momentum back within the safe region, avoiding saturation.

Figure 2 illustrates the relationship between the soft constraint and the operational limits of the RWs. The original hard limits h_{\max} and h_{\min} define the absolute, physically-imposed boundaries that cannot be violated. The soft constraint bounds h_{\max}^{soft} and h_{\min}^{soft} define the preferred operating limits. The light blue area defined by $h_{\min}^{\text{soft}} \leq h \leq h_{\max}^{\text{soft}}$ is the region where the soft constraint is satisfied and the slack variable α is zero and has no effect on the MPC objective function. The light red area defined by $h_{\max}^{\text{soft}} \leq h$ or $h \leq h_{\min}^{\text{soft}}$ is the region where the soft constraint is violated. When the MPC design variable enters this region, the slack variable α takes on a positive value and the violation is heavily penalized in the objective function. Two examples of design variable sequence interpreting the design choices in the MPC optimization are shown in Fig. 2. The red trajectory (labeled as “MPC design 1”) represents an action that violates the soft constraint in the first two steps, incurring a large penalty due to the quadratic weight on the slack variable in the MPC objective function. The blue trajectory (labeled as “MPC design 2”) represents a sequence of design that remains within the feasible region, incurring no penalty within the MPC objective function.

The soft constraint serves to improve feasibility of the MPC optimization problem by penalizing, rather than prohibiting, constraint violation. This structure strongly discourages the design variables from exceeding the soft bounds $h_{\max}^{\text{soft}} \leq h \leq h_{\min}^{\text{soft}}$, but allows for excursions outside this region if the performance benefit outweighs the imposed penalty.

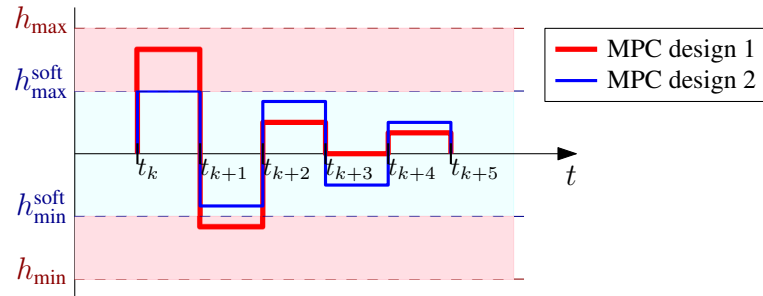


Figure 2: Illustration of the MPC soft constraint design with a prediction horizon of $N = 5$, where no penalty is incurred for responses satisfying $h_{\min}^{\text{soft}} \leq h \leq h_{\max}^{\text{soft}}$, while a quadratic penalty appears in the MPC objective function when $h_{\max}^{\text{soft}} \leq h$ or $h \leq h_{\min}^{\text{soft}}$. The response labeled “MPC design 1” indicates a design that violates the soft constraint, while “MPC design 2” does not.

4.4. Input Constraints

To ensure actuator feasibility and the satisfaction of hardware limits, constraints are imposed on both the control input magnitude and the rate of AMT motion. The actuator input vector $\mathbf{u}_{j|t_k}$ is subject to the constraints $\mathbf{u}_{\min} \leq \mathbf{u}_{j|t_k} \leq \mathbf{u}_{\max}$, where the bounds $\mathbf{u}_{\min} = [\mathbf{u}_{\min}^{\text{AMT}^T} \quad u_{\min}^{\text{RCD}}]^T$ and $\mathbf{u}_{\max} = [\mathbf{u}_{\max}^{\text{AMT}^T} \quad u_{\max}^{\text{RCD}}]^T$ reflect the physical actuation limits of the AMT and RCDs.

In addition, the translational rate of the AMT is constrained to avoid unrealistic or dynamically infeasible actuation commands, referring to the physical speed limit of AMT. Due to the discrete-time formulation of the MPC problem, the rate constraint is implemented as a finite difference inequality

$$\dot{\mathbf{u}}_{\min}^{\text{AMT}} \leq \frac{\mathbf{u}_{j|t_k}^{\text{AMT}} - \mathbf{u}_{j-1|t_k}^{\text{AMT}}}{\Delta t} \leq \dot{\mathbf{u}}_{\max}^{\text{AMT}},$$

where $\dot{\mathbf{u}}_{\min}^{\text{AMT}}$ and $\dot{\mathbf{u}}_{\max}^{\text{AMT}}$ define the allowable lower and upper bounds on the AMT velocity.

To ensure input continuity across successive control intervals, which is critical for the AMT input between discrete time steps, the initial AMT input at each new MPC update must match the current AMT position. This continuity constraint is enforced as $\mathbf{u}_{-1|t_k}^{\text{AMT}} = \mathbf{u}^{\text{AMT}}(t_k)$, where the current AMT position becomes a design variable fixed by this equality constraint and is used to constrain the AMT rate of the first input within the MPC optimization problem. This formulation ensures smooth AMT motion while preserving the predictive accuracy and numerical stability of the MPC framework.

4.5. Objective Function

The objective function of the proposed MPC policy is formulated to balance state regulation, actuator efficiency, AMT motion minimization, and enforcement of soft constraints. It is defined as

$$\sum_{j=0}^{N-1} \left(\mathbf{x}_{j|t_k}^{\text{MPC}^T} \mathbf{Q} \mathbf{x}_{j|t_k}^{\text{MPC}} + \mathbf{u}_{j|t_k}^T \mathbf{R} \mathbf{u}_{j|t_k} + \tilde{\mathbf{u}}_{j|t_k}^{\text{AMT}^T} \tilde{\mathbf{R}} \tilde{\mathbf{u}}_{j|t_k}^{\text{AMT}} \right) + \mathbf{x}_{N|t_k}^{\text{MPC}^T} \mathbf{Q}_N \mathbf{x}_{N|t_k}^{\text{MPC}} + \boldsymbol{\alpha}^T \mathbf{C} \boldsymbol{\alpha},$$

where $\mathbf{x}_{j|t_k}^{\text{MPC}}$ and $\mathbf{u}_{j|t_k} = [\mathbf{u}_{j|t_k}^{\text{AMT}^T} \quad u_{j|t_k}^{\text{RCD}}]^T$ denote the predicted state and control input at stage j over the prediction horizon of length N ; $\mathbf{Q} = \mathbf{Q}^T$ and $\mathbf{R} = \mathbf{R}^T$ are positive semi-definite and positive definite weighting matrices, respectively, penalizing the state and control input; \mathbf{Q}_N is the terminal weighting matrix for the final predicted state at stage N ; $\mathbf{C} = \mathbf{C}^T$ is a positive semi-definite matrix that penalizes violation of the soft constraint via the slack variable $\boldsymbol{\alpha} \geq \mathbf{0}$; $\tilde{\mathbf{R}} = \tilde{\mathbf{R}}^T$ is a positive semi-definite matrix penalizing the rate of AMT translation; and $\tilde{\mathbf{u}}_{j|t_k}^{\text{AMT}} = \mathbf{u}_{j|t_k}^{\text{AMT}} - \mathbf{u}_{j-1|t_k}^{\text{AMT}}$ is the difference between the j -th AMT input and the previous input.

The term $\tilde{\mathbf{u}}_{j|t_k}^{\text{AMT}^T} \tilde{\mathbf{R}} \tilde{\mathbf{u}}_{j|t_k}^{\text{AMT}}$ is included to discourage unnecessary movement of the AMT, thereby promoting actuator efficiency and helping maintain the AMT in a relatively stationary configuration across time steps. This is particularly important given the discretized AMT inputs and the associated mechanical and dynamic constraints. The slack variable penalty $\boldsymbol{\alpha}^T \mathbf{C} \boldsymbol{\alpha}$ enables soft constraint enforcement on RW angular momentum, where violations are permitted when necessary, but discouraged through a quadratic penalty.

4.6. Summary of MPC Policy and Implementation Details

The proposed MPC policy involves solving for the optimization problem

$$\underset{\mathcal{X}, \mathcal{U}, \alpha}{\text{minimize}} \sum_{j=0}^{N-1} \left(\mathbf{x}_{j|t_k}^{\text{MPC}^\top} \mathbf{Q} \mathbf{x}_{j|t_k}^{\text{MPC}} + \mathbf{u}_{j|t_k}^\top \mathbf{R} \mathbf{u}_{j|t_k} + \tilde{\mathbf{u}}_{j|t_k}^{\text{AMT}^\top} \tilde{\mathbf{R}} \tilde{\mathbf{u}}_{j|t_k}^{\text{AMT}} \right) + \mathbf{x}_{N|t_k}^{\text{MPC}^\top} \mathbf{Q}_N \mathbf{x}_{N|t_k}^{\text{MPC}} + \alpha^\top \mathbf{C} \alpha \quad (13)$$

subject to

$$\begin{aligned} \mathbf{x}_{j+1|t_k}^{\text{MPC}} &= \mathbf{A}_k^{\text{MPC}} \mathbf{x}_{j|t_k}^{\text{MPC}} + \mathbf{B}_{w,k}^{\text{MPC}} \mathbf{w}_{j|t_k} + \mathbf{B}_{u1,k}^{\text{MPC}} \mathbf{u}_{j|t_k}^{\text{AMT}} + \mathbf{B}_{u2,k}^{\text{MPC}} \mathbf{u}_{j|t_k}^{\text{RCD}}, \quad j = 0, 1, \dots, N-1, \\ \mathbf{x}_{0|t_k}^{\text{MPC}} &= \mathbf{x}^{\text{MPC}}(t_k), \\ \mathbf{u}_{-1|t_k}^{\text{AMT}} &= \mathbf{u}^{\text{AMT}}(t_k), \\ \mathbf{x}_{\min}^{\text{MPC}} &\leq \mathbf{x}_{j|t_k}^{\text{MPC}} \leq \mathbf{x}_{\max}^{\text{MPC}}, \quad j = 0, \dots, N, \\ \mathbf{u}_{\min} &\leq \mathbf{u}_{j|t_k} \leq \mathbf{u}_{\max}, \quad j = 0, \dots, N-1, \\ \dot{\mathbf{u}}_{\min}^{\text{AMT}} &\leq \frac{\mathbf{u}_{j|t_k}^{\text{AMT}} - \mathbf{u}_{j-1|t_k}^{\text{AMT}}}{\Delta t} \leq \dot{\mathbf{u}}_{\max}^{\text{AMT}}, \quad j = 0, \dots, N-1, \\ \mathbf{h}_{4,\min}^{\text{soft}} - \alpha &\leq \mathbf{h}_{4,j|t_k}^{\text{RW}} \leq \mathbf{h}_{4,\max}^{\text{soft}} + \alpha, \quad j = 0, \dots, N, \\ \alpha &\geq \mathbf{0}, \end{aligned}$$

where $\alpha \in \mathbb{R}^4$, $\mathcal{X} = \{\mathbf{x}_{0|t_k}^{\text{MPC}}, \mathbf{x}_{1|t_k}^{\text{MPC}}, \dots, \mathbf{x}_{N|t_k}^{\text{MPC}}\}$, $\mathcal{U} = \{\mathbf{u}_{-1|t_k}, \mathbf{u}_{0|t_k}, \mathbf{u}_{1|t_k}, \dots, \mathbf{u}_{N-1|t_k}\}$ are the design variables, N is the number of timesteps in the prediction horizon, $\mathbf{x}^{\text{MPC}}(t_k)$ is the known system state at time t_k , and $\mathbf{u}^{\text{AMT}}(t_k)$ is the AMT position at time t_k .

Due to the use of a quadratic objective function, affine equality constraints, and affine inequality constraints, this MPC policy can be solved as a QP at each time step. Solving this problem yields a sequence of optimal control inputs over the prediction horizon, i.e., $\mathcal{U}^* = \{\mathbf{u}_{-1|t_k}^*, \mathbf{u}_{0|t_k}^*, \mathbf{u}_{1|t_k}^*, \dots, \mathbf{u}_{N-1|t_k}^*\}$. Only the first input ($\mathbf{u}_{0|t_k}^*$) is applied to the system before proceeding to the next time step and again solving for the optimal sequence of control inputs.

In this work, the Kalman filter is designed to operate at the same rate (every 100 seconds) as the MPC momentum management time step. At every time step t_k , a measurement update is performed, and the Kalman filter state $\hat{\mathbf{X}}_k^+ = \begin{bmatrix} \hat{\mathbf{x}}_k^+ \\ \hat{\mathbf{w}}_k^+ \end{bmatrix}$ is extracted to formulate the MPC prediction model in Eq. (12), where $\mathbf{x}_k = \hat{\mathbf{x}}_k^+$ and $\mathbf{w}_k = \hat{\mathbf{w}}_k^+$ are used for the prediction model at time t_k , and the linear transformation \mathbf{T} is used to compute $\mathbf{x}_k^{\text{MPC}}$, where $\mathbf{x}_k^{\text{MPC}} = \mathbf{T} \mathbf{x}_k$. This transformation enables MPC to seek a minimum norm angular momentum allocation while directly constraining the angular momentum on each RW.

The recursive nature of the MPC necessitates the prediction model to be re-linearized about the current state and inputs at every time step. To improve actuation efficiency and mitigate noise, operational actuation thresholds on the AMT and RCDs are introduced as additional design tuning parameters. These thresholds are designed to trim out minor control demands, removing small AMT movements and RCD thrusts that typically arise from minor momentum management or noisy state estimates. Specifically, any element of the MPC-demanded AMT position change satisfying the element-wise inequality $|\mathbf{u}_{0|t_k}^{\text{AMT}} - \mathbf{u}_{-1|t_k}^{\text{AMT}}| / \Delta t \leq \beta_{\text{thresh}}^{\text{AMT}} \dot{\mathbf{u}}_{\max}^{\text{AMT}}$ is set to stay at its current position ($\mathbf{u}_{0|t_k}^{\text{AMT}} = \mathbf{u}_{-1|t_k}^{\text{AMT}}$) for the upcoming time step. Additionally, if the MPC-demanded RCD input satisfies $|\mathbf{u}_{0|t_k}^{\text{RCD}}| < \beta_{\text{thresh}}^{\text{RCD}} \mathbf{u}_{\max}^{\text{RCD}}$, then it is set to zero. In both cases, the control input is applied to the system only when the MPC demands an input exceeding the predefined magnitude thresholds. The momentum management inputs filtered by the thresholds are then passed to perform the time update of the Kalman filter, and applied to the system.

Since the MPC demanded RCD input is a continuous value between $\pm \tau_{b3,\text{on}}^{\text{RCD}}$, it does not directly match the on-off actuation mechanism of the RCD array. A single pulse PWM-quantization technique in Eq. (8) is used to turn the continuous RCD input value to a pulse length specified time with $\tau_{b3,\text{on}}^{\text{RCD}}$ value. These thresholding filter and PWM-quantization are leveraging the MPC recursive nature. Once an input is trimmed or modified at one time step, the MPC recalculates the optimal inputs using the latest state at the next time step, compensating for the mismatched input and system dynamics.

5. Numerical Simulation Results

Numerical simulation experiments are performed to validate the MPC momentum management policy on Solar Cruiser. Section 5.1 presents the setup of the system and the controller. Section 5.2 presents the state-of-the-art thresh-

olding momentum management control developed for NASA's Solar Cruiser by Inness et al. (2023); Tyler et al. (2023), which is used as a validation of the simulation environment and a benchmark comparison to the proposed method. Section 5.3 presents simulations of the proposed MPC momentum management policy under different conditions, exhibiting the importance of incorporating a disturbance estimate with the MPC policy and the effect that threshold design has on actuator efficiency. Section 5.4 presents a direct comparison of the proposed MPC-based momentum management and the state-of-the-art NASA's thresholding method.

5.1. Simulation Setup

The simulation parameters are chosen to reflect NASA's Solar Cruiser (Johnson et al., 2019; Johnson and Curran, 2020; Tyler et al., 2023; Inness et al., 2023). The total mass of the sailcraft is 111 kg, where the bus and the sail each contribute half of the total mass. The out-of-plane offset between the CM and the sail surface (also the CP) is captured by r_{b3}^{ps} , the third component of $\mathbf{r}_b^{ps}(t)$. Unlike the simulations performed by Shen and Caverly (2025b) that assumed this offset to be zero, this distance is chosen as $r_{b3}^{ps} = 0.47$ m in this paper to more accurately simulate Solar Cruiser's geometry. The configuration of the 4-RW pyramid is given by $\psi_i = 60^\circ$ for all i , $\phi_i = 45^\circ + (i-1) \cdot 90^\circ$ for $i = 1, 2, 3, 4$, resulting in the mapping matrix given in Eq. 3. The RWs perform attitude tracking using the PID control law in Eq. (2) with gains $\mathbf{K}_p = 0.25 \cdot \mathbf{1}_{3 \times 3}$ N·m/rad, $\mathbf{K}_d = 112 \cdot \mathbf{1}_{3 \times 3}$ N·m/s/rad, $\mathbf{K}_i = 8 \times 10^{-4} \cdot \mathbf{1}_{3 \times 3}$ N·m/(rad·s). The rest of Solar Cruiser's physical parameters are included in Table 1. The SRP force $\mathbf{f}_b^{\text{SRP}} = [0.0003 \ 0 \ 0.013]^\top$ N is computed assuming Solar Cruiser is at 1 au and a 0° clock angle, and has the non-ideal reflectivity properties outlined by Heaton and Artusio-Glimpse (2015), while the disturbance torque is chosen based on the worst-case deformed sail shapes investigated by Gauvain and Tyler (2023). The disturbance torque $\tau_b^{\text{dist}} = [8 \ 8 \ 0.2]^\top \times 10^{-4}$ N·m assumes a constant environmental force and torque as representative of a worst-case disturbance scenario for the Solar Cruiser under a 17° SIA (Inness et al., 2023). While a disturbance of such a magnitude is unlikely to persist throughout a practical mission, it provides a conservative estimate for validating the robustness of the proposed controller. The SRP force is assumed to be perfectly known from the onboard ADCS and guidance system, and is used in the MPC prediction model formulation. The simulation and attitude control timestep is $dt = 1$ second, and the momentum management time step is $\Delta t = 100$ seconds.

The AMT has a translation limit of $\mathbf{u}_{\max}^{\text{AMT}} = -\mathbf{u}_{\min}^{\text{AMT}} = [0.29 \ 0.29]^\top$ m and a rate limit of $\dot{\mathbf{u}}_{\max}^{\text{AMT}} = -\dot{\mathbf{u}}_{\min}^{\text{AMT}} = [0.5 \ 0.5]^\top$ mm/s in the $\overset{\rightarrow}{b^1}$ and $\overset{\rightarrow}{b^2}$ axes (Johnson and Curran, 2020). The discrete-time rate constraint is defined as $\dot{\mathbf{u}}_{\max}^{\text{AMT}} = -\dot{\mathbf{u}}_{\min}^{\text{AMT}} = (\mathbf{u}_{j+1|k}^{\text{AMT}} - \mathbf{u}_{j|k}^{\text{AMT}})/\Delta t$, which limits the maximum AMT position change to be 0.05 m in each axis at every momentum management time step. The roll torque generated when the RCDs are turned on is set to meet the Solar Cruiser's roll torque requirement at 6.525×10^{-5} N·m, which is 1.5 times the sum of worst case roll disturbance and AMT induced roll torque at its maximum position offset (Heaton et al., 2023; Johnson et al., 2022).

The Kalman filter measurement noise covariance is chosen based on NASA Solar Cruiser's performance requirement (Johnson and Curran, 2020). It is assumed that the onboard ADCS measurement noise standard deviation is 3 times smaller (more accurate) than the control requirement defined by Johnson and Curran (2020). Based on the required pointing accuracy of < 60 arcsec in pitch/yaw and < 6.8 arcmin in roll (3σ), the 1σ attitude measurement accuracy is chosen as 0.00186° in pitch/yaw and 0.0125° in roll, i.e., $\sigma_\theta = \text{diag}(0.00186^\circ, 0.00186^\circ, 0.0125^\circ)$.

Table 1: System parameters used in the numerical simulations.

Parameter	Value	Units
m_p	55.5	kg
m_s	55.5	kg
$\mathbf{J}_b^{\mathcal{P}_p}$	$\text{diag}(4.01, 4.01, 6.07)$	kg·m ²
\mathbf{J}_b^{Ss}	$\text{diag}(8049.8, 8049.8, 16099.6)$	kg·m ²
r_w	0.11	m
r_{b3}^{ps}	0.47	m
$\mathbf{f}_b^{\text{SRP}}$	$[0.0003 \ 0 \ 0.013]^\top$	N
τ_b^{dist}	$[8 \ 8 \ 0.2]^\top \times 10^{-4}$	N·m
\mathbf{K}_p	$0.25 \cdot \mathbf{1}_{3 \times 3}$	N·m/rad
\mathbf{K}_d	$112 \cdot \mathbf{1}_{3 \times 3}$	N·m·s/rad
\mathbf{K}_i	$8 \times 10^{-4} \cdot \mathbf{1}_{3 \times 3}$	N·m/(rad·s)

Table 2: Kalman filter estimation tuning parameters used in the numerical simulations.

Parameter	Value	Unit
σ_θ	$\text{diag}(1.86, 1.86, 12.5) \cdot 10^{-3}$	deg
σ_ω	$\text{diag}(3.06, 3.06, 25) \cdot 10^{-4}$	deg/s
σ_h	$10^{-5} \cdot \mathbf{1}_{3 \times 3}$	N·m·s
σ_e	$10^{-8} \cdot \mathbf{1}_{3 \times 3}$	rad·s
σ_h	$10^{-4} \cdot \mathbf{1}_{3 \times 3}$	N·m
\mathbf{q}_θ	$0.01^2 \cdot \mathbf{1}_{3 \times 3}$	deg ²
\mathbf{q}_ω	$0.0001^2 \cdot \mathbf{1}_{3 \times 3}$	(deg/s) ²
\mathbf{q}_h	$(10^{-3})^2 \cdot \mathbf{1}_{3 \times 3}$	(N·m·s) ²
\mathbf{q}_e	$(10^{-8})^2 \cdot \mathbf{1}_{3 \times 3}$	(rad·s) ²
$q_{\tau 1} = q_{\tau 2} = q_{\tau 3}$	$(5 \times 10^{-5})^2$	(N·m) ²
\mathbf{R}^{KF}	$\text{diag}(\sigma_\theta^2, \sigma_\omega^2, \sigma_h^2, \sigma_e^2, \sigma_h^2)$	
$\mathbf{Q}_{\text{model}}^{\text{KF}}$	$\text{diag}(\mathbf{q}_\theta, \mathbf{q}_\omega, \mathbf{q}_h, \mathbf{q}_e)$	
$\mathbf{Q}_{\text{dist}}^{\text{KF}}$	$\text{diag}(q_{\tau 1}, q_{\tau 2}, q_{\tau 3})$	

Based on the pointing jitter requirements of < 10 arcsec/sec in pitch/yaw and < 1.34 arcmin/sec in roll (3σ), the 1σ angular rate measurement accuracy is chosen as 0.000306 deg/sec in pitch/yaw and 0.0025 deg/sec in roll, i.e., $\sigma_\omega = \text{diag}(0.000306, 0.000306, 0.0025)$ deg/sec. It is assumed that the RW angular momentum measurement accuracy is $\sigma_h = 10^{-5} \cdot \mathbf{1}_{3 \times 3}$ N·m·s, and $\sigma_e = 10^{-8} \cdot \mathbf{1}_{3 \times 3}$ rad·s, as these parameters are not publicly available in the literature. The measurement of \mathbf{h}^{RW} is associated to the RW torque accuracy, which is assumed to have roughly the same magnitude of accuracy as ω_b^{ba} , thus, $\sigma_h = 10^{-4} \cdot \mathbf{1}_{3 \times 3}$ N·m. The collective measurement noise covariance is given by $\mathbf{R}^{\text{KF}} = \text{diag}(\mathbf{r}_\theta, \mathbf{r}_\omega, \mathbf{r}_h, \mathbf{r}_e, \mathbf{r}_h) = \text{diag}(\sigma_\theta^2, \sigma_\omega^2, \sigma_h^2, \sigma_e^2, \sigma_h^2)$. In the simulation, zero-mean Gaussian white noise with the same measurement covariance is added to each of the measurement parameters in Kalman filter measurement update step.

The Kalman filter process noise covariance is given by $\mathbf{Q}^{\text{KF}} = \text{diag}(\mathbf{Q}_{\text{model}}^{\text{KF}}, \mathbf{Q}_{\text{dist}}^{\text{KF}})$, which is largely a tuning parameter of the filter. The dynamic model error covariance $\mathbf{Q}_{\text{model}}^{\text{KF}} = \text{diag}(0.01^2 \cdot \mathbf{1}_{3 \times 3}, 0.0001^2 \cdot \mathbf{1}_{3 \times 3}, 10^{-6} \cdot \mathbf{1}_{3 \times 3}, 10^{-16} \cdot \mathbf{1}_{3 \times 3})$, whose units are deg², deg²/s², (N·m·s)², and (rad·s)², characterizes the combination of linearization error in the dynamics and expected deviations in the trajectory. The disturbance model error covariance $\mathbf{Q}_{\text{dist}}^{\text{KF}} = (5 \times 10^{-5})^2 \cdot \mathbf{1}_{3 \times 3}$ N·m² is chosen to characterize the slowly-varying nature of the disturbance estimate and the other model discrepancies captured by $\hat{\mathbf{w}}$. The initial state estimate $\hat{\mathbf{X}}_0^- = \mathbf{0}$ does not consider any preliminary information of the state and disturbance error. The initial estimation error covariance is chosen as $\mathbf{P}_0^- = \text{diag}(2000\mathbf{q}_\theta, 200\mathbf{q}_\omega, 200\mathbf{q}_h, 200\mathbf{q}_e, 200\mathbf{Q}_{\text{dist}}^{\text{KF}})$. A summary of the numerical parameters used within the Kalman filter is provided in Table 2.

In this work, the Kalman filter operates at the same frequency as the momentum management system, which has a time step of 100 seconds. The system undergoes a initial slew of attitude tracking, and the Kalman filter acquires its first measurement update at the first momentum management timestep, i.e., $t_k = 100$ sec. After the measurement update, the momentum management policy determines the associated AMT and RCD inputs, which are then used in the time update using the Kalman filter process model. The momentum management inputs are applied to the nonlinear dynamics as in Eq. (1) until the next momentum management timestep, the process of a measurement update, momentum management input determination, time update, and application of the input to the nonlinear system is repeated.

5.2. NASA's State-of-the-art Method

NASA's state-of-the-art momentum management strategy used on Solar Cruiser is establishes as a benchmark comparison to the proposed MPC strategy. The Solar Cruiser momentum management system utilizes three threshold-based decoupled channels to command the AMT and RCDs (Inness et al., 2023; Tyler et al., 2023). Solar Cruiser employs on-off thresholds for both AMT and RCD activation, which are based on the RWs' stored angular momentum in the pitch/yaw and roll axes. An upper activation threshold is set higher than a lower deactivation threshold, establishing a hysteresis. Specifically, an actuator engages only when its corresponding RW momentum exceeds the activation threshold and remains active until the momentum drops below the deactivation threshold.

The two AMT axes (pitch and yaw) are controlled independently via PID control laws, which regulate the accumu-

lated angular momentum stored in the corresponding RWs. The control laws for the two axes are defined as

$$u_1^{\text{AMT}} = K_p^{\text{AMT}} h_{b2}^{\text{RW}} + K_d^{\text{AMT}} \dot{h}_{b2}^{\text{RW}} + K_i^{\text{AMT}} \int_{t_0}^t h_{b2}^{\text{RW}}(\tau) d\tau,$$

$$u_2^{\text{AMT}} = -K_p^{\text{AMT}} h_{b1}^{\text{RW}} - K_d^{\text{AMT}} \dot{h}_{b1}^{\text{RW}} - K_i^{\text{AMT}} \int_{t_0}^t h_{b1}^{\text{RW}}(\tau) d\tau.$$

The sign difference between the two PID control laws reflects the dynamics in Eq. (1), where the AMT-induced torque $\tau_b^{\text{AMT}} = \frac{m_s}{m_p + m_s} \mathbf{r}_b^{ps^*} \mathbf{f}_b^{\text{SRP}}$ involves a cross product with opposite signs along the body 1 and 2 axes. This control input is updated with a time step of $\Delta t = 100$ sec using a ZOH to maintain a constant command throughout the interval. The RCDs' actuation follows a simple on-off logic with a fixed torque magnitude when activated. The RCD activation/deactivation switch aligns with the momentum management time step Δt .

This threshold-based control, along with the AMT PID gains, is tuned via simulation to optimize performance. Crucially, this PID control framework does not inherently account for physical actuator constraints, such as AMT position and rate limits. These limits are enforced externally after the PID controller determines the position command. Consequently, tuning the controller to ensure effective momentum management while avoiding actuator saturation remains a key design challenge.

In the absence of any numerical values in the work of Inness et al. (2023); Tyler et al. (2023), values are chosen in this paper in an attempt to recreate the results of Inness et al. (2023); Tyler et al. (2023). To this end, the chosen thresholds for the AMT are 0.125 N·m·s for activation, and 0.0312 N·m·s for deactivation. The PID gains of the AMT controller are chosen as $K_p^{\text{AMT}} = 0.4$ (N·s) $^{-1}$, $K_d^{\text{AMT}} = 0.4$ N $^{-1}$, and $K_i^{\text{AMT}} = 0.0002$ N $^{-1}$ s $^{-2}$. The maximum position constraint of the AMT is enforced such that $|u_i^{\text{AMT}}| = u_{i,\text{max}}^{\text{AMT}} = 0.29$ m when the determined PID controller input satisfies $|u_i^{\text{AMT}}| > u_{i,\text{max}}^{\text{AMT}}$ ($i = 1, 2$). The maximum AMT rate constraint is enforced such that $|u_i^{\text{AMT}}| = \Delta t \cdot \dot{u}_{i,\text{max}}^{\text{AMT}} = 0.05$ m when the determined PID input satisfies $|u_i^{\text{AMT}}| > \Delta t \cdot \dot{u}_{i,\text{max}}^{\text{AMT}}$ ($i = 1, 2$). The chosen RCD thresholds are 0.25 N·m·s for activation, and 0.125 N·m·s for deactivation.

For practicality and for a fair comparison to the proposed method, the threshold-based momentum management uses state estimates from the Kalman filter to determine AMT and RCD inputs. Specifically, the angular momentum estimate $\hat{\mathbf{h}}_{b,k}^{\text{RW}^+}$ is used to assess the activation/deactivation threshold and AMT proportional control, and $\hat{\mathbf{h}}_{b,k}^{\text{RW}^+} = \mathbf{K}_p(\hat{\theta}_k^+ - \theta_d) + \mathbf{K}_d(\omega_{b,k}^{ba^+} - \dot{\theta}_d) + \mathbf{K}_i \mathbf{e}^{\text{int}^+}$ is used for the AMT derivative control. For the AMT integral control, it is assumed that a perfect measurement of $\int_{t_0}^t \mathbf{h}_b^{\text{RW}}(\tau) d\tau$ is accessible in the ADCS.

Using NASA's state-of-the-art thresholding momentum management policy, a slew maneuver tracking initial attitude of $\theta_0 = [-3^\circ \ 0 \ 0]^\top$ to $\theta_d = \mathbf{0}$ is performed. As shown in Fig. 3 with the label "NASA-3," the 3° slew demonstrates effective momentum management, where the performance is similar to that shown by Inness et al. (2023); Tyler et al. (2023), although this is difficult to compare quantitatively due to redacted plot axes. The momentum management method developed by Inness et al. (2023); Tyler et al. (2023) is effective at keeping the angular momentum of the RWs within reasonable bounds with realistic actuation inputs. However, with a slightly larger slew maneuver starting from $\theta_0 = [-4^\circ \ 0 \ 0]^\top$, the system suffers from RW saturation, and the solar sail loses attitude control authority, which is shown in the result of Fig. 3 with the label "NASA-4." For reference, the black dashed lines in Fig. 3(b) indicate 25% of the angular momentum capacity of each RW, which is also the soft constraint value chosen for the proposed MPC-based approach in the following sections. The black dashed lines in Fig. 3(c) indicate the activation thresholds, while the green dashed lines represent the deactivation thresholds.

5.3. Proposed MPC-based Momentum Management Supported by KF Disturbance Estimate

While Solar Cruiser's momentum management method failed to desaturate the RWs and eventually lost attitude control when performing the larger slew, the proposed MPC-based momentum management strategy has the potential to foresee the upcoming angular momentum growth and proactively take actions. This allows for more aggressive slews while maintaining RW control authority.

To highlight this improved performance, simulations of a larger slew maneuver are performed, regulating from $\theta_0 = [-6^\circ \ 0 \ 0]^\top$ to $\theta_d = \mathbf{0}$ with the RW PID control law, while the stored RW angular momentum is unloaded by the momentum management MPC policy outlined in Section 4. The system parameters and Kalman filter parameters are the same as presented in Section 5.1. The MPC prediction horizon is chosen as $N = 10$ timesteps, corresponding to a 1000 sec forecast. The state constraints in MPC are determined by mission requirements and RW limits, with the

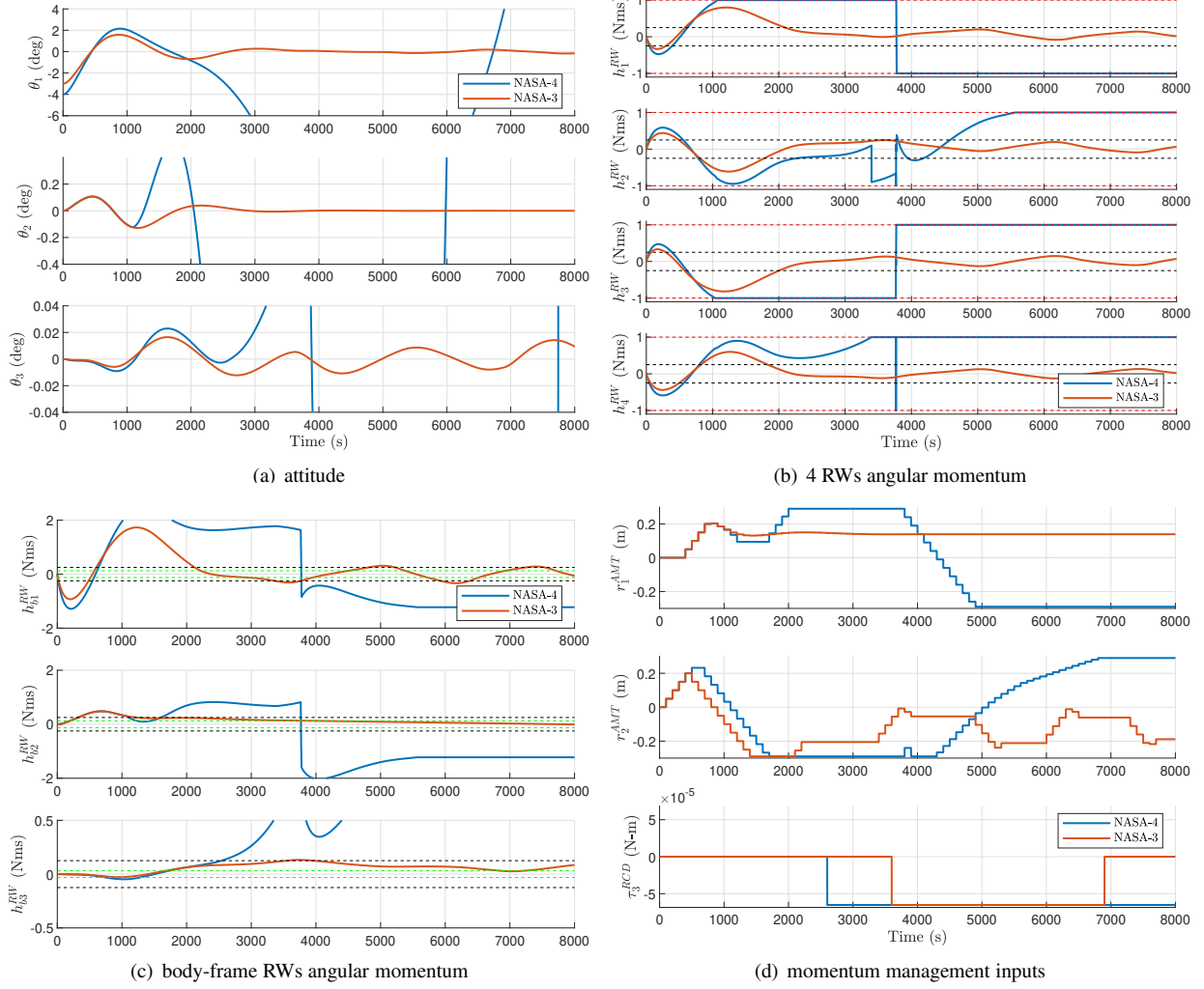


Figure 3: Simulation results using NASA’s Solar Cruiser momentum management strategy from Inness et al. (2023); Tyler et al. (2023), featuring RW saturation under a 4° slew compared to a 3° slew. The black dashed line in (c) denotes the activation threshold (50% of the soft constraint in MPC), and the green dashed line denotes the deactivation threshold (50% of the activation threshold).

attitude limit $\theta_{\max} = -\theta_{\min} = [20^\circ \ 20^\circ \ 20^\circ]^\top$, the angular rate limit $\omega_{b,\max}^{ba} = -\omega_{b,\min}^{ba} = [0.1 \ 0.1 \ 0.1]^\top$ deg/s, the RW angular momentum capacity $\mathbf{h}_{4,\max}^{\text{RW}} = -\mathbf{h}_{4,\min}^{\text{RW}} = [1 \ 1 \ 1 \ 1]^\top$ N·m·s, and a large PID integral term $\mathbf{e}_{\max}^{\text{int}} = -\mathbf{e}_{\min}^{\text{int}} = [10^6 \ 10^6 \ 10^6]^\top$ rad·s as an internal state limit. The attitude and angular rate constraints are set to arbitrarily large limits for design completeness and flexibility, ensuring the framework can accommodate future mission requirements that may involve more aggressive maneuvers. The soft constraint limits are chosen as 25% of the RWs angular momentum capacity, i.e., $\mathbf{h}_{4,\max}^{\text{soft}} = 0.25 \cdot \mathbf{h}_{4,\max}^{\text{RW}}$ and $\mathbf{h}_{4,\min}^{\text{soft}} = -\mathbf{h}_{4,\max}^{\text{soft}}$. The slack variable $\alpha \geq 0$ is penalized heavily by the weighting matrix $\mathbf{C} = 10000 \cdot \mathbf{1}_{4 \times 4}$ in the objective function when $\mathbf{h}_{4,j|t_k}^{\text{RW}}$ deviates from the soft constraint envelope. The weights in the MPC objective function are provided in Table 3, which are parameters that can be tuned to tailor the performance objective to different mission stages and scenarios.

It is worth noting that the MPC evaluates RCD inputs as continuous values between u_{\min}^{RCD} and u_{\max}^{RCD} , but the actual applied input is quantized into the full on/off value with pulse length t_c using PWM quantization as in Eq. (8).

To demonstrate the importance of disturbance knowledge in the MPC framework, simulation results with and without the Kalman filter disturbance estimate knowledge in MPC are shown in Fig. 4, where no threshold is used ($\beta_{\text{thresh}}^{\text{AMT}} = \beta_{\text{thresh}}^{\text{RCD}} = 0$). The result in blue labeled “nominal MPC” uses the nominal MPC implementation without disturbance knowledge, where the MPC prediction model uses $\mathbf{w}_{j|t_k} = \mathbf{0}$, for $j = 0, 1, \dots, N - 1$. The result in

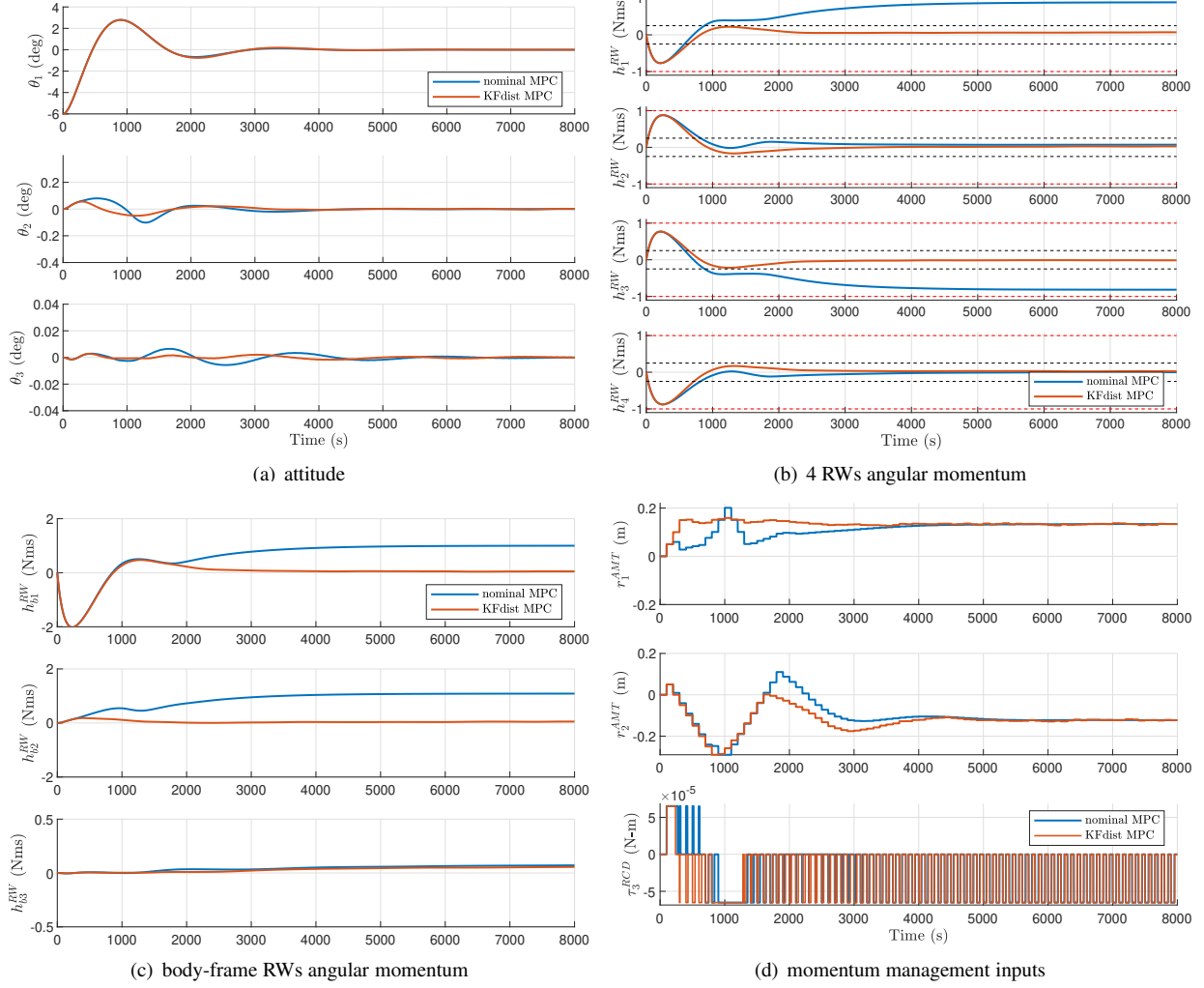


Figure 4: Simulation results using the proposed MPC momentum management strategy under a 6 deg slew with and without (nominal) the disturbance estimate knowledge in prediction model. The black dashed lines in (b) denote the 25% soft constraint on 4-RWs angular momentum.

red labeled ‘‘KFdist MPC’’ includes the Kalman filter estimate disturbance within the MPC prediction model, where $\mathbf{w}_{j|k} = \hat{\mathbf{w}}_k^+$, for $j = 0, 1, \dots, N - 1$. Although both of the MPC policies perform successful momentum management under a 6° slew, the nominal MPC results in the angular momentum of two RWs stabilizing near their saturation limits. Conversely, the MPC implementation incorporating the disturbance estimate exhibits a significant performance improvement, driving all RW angular momentum down to values safely within the specified soft constraint boundaries, thereby reserving greater control authority.

An additional actuation threshold can be applied on the MPC inputs to filter out minor actuation with minimal loss

Table 3: MPC tuning parameters used in the numerical simulations.

Parameter	Value
N	10
\mathbf{Q}	$\text{diag}(10 \cdot \mathbf{1}_{6 \times 6}, 0.5 \cdot \mathbf{1}_{4 \times 4}, \mathbf{0}_{3 \times 3})$
\mathbf{Q}_N	$\mathbf{1}_{13 \times 13}$
\mathbf{R}	$\text{diag}(1, 1, 10^6)$
$\tilde{\mathbf{R}}$	$100 \cdot \mathbf{1}_{2 \times 2}$
\mathbf{C}	$10000 \cdot \mathbf{1}_{4 \times 4}$

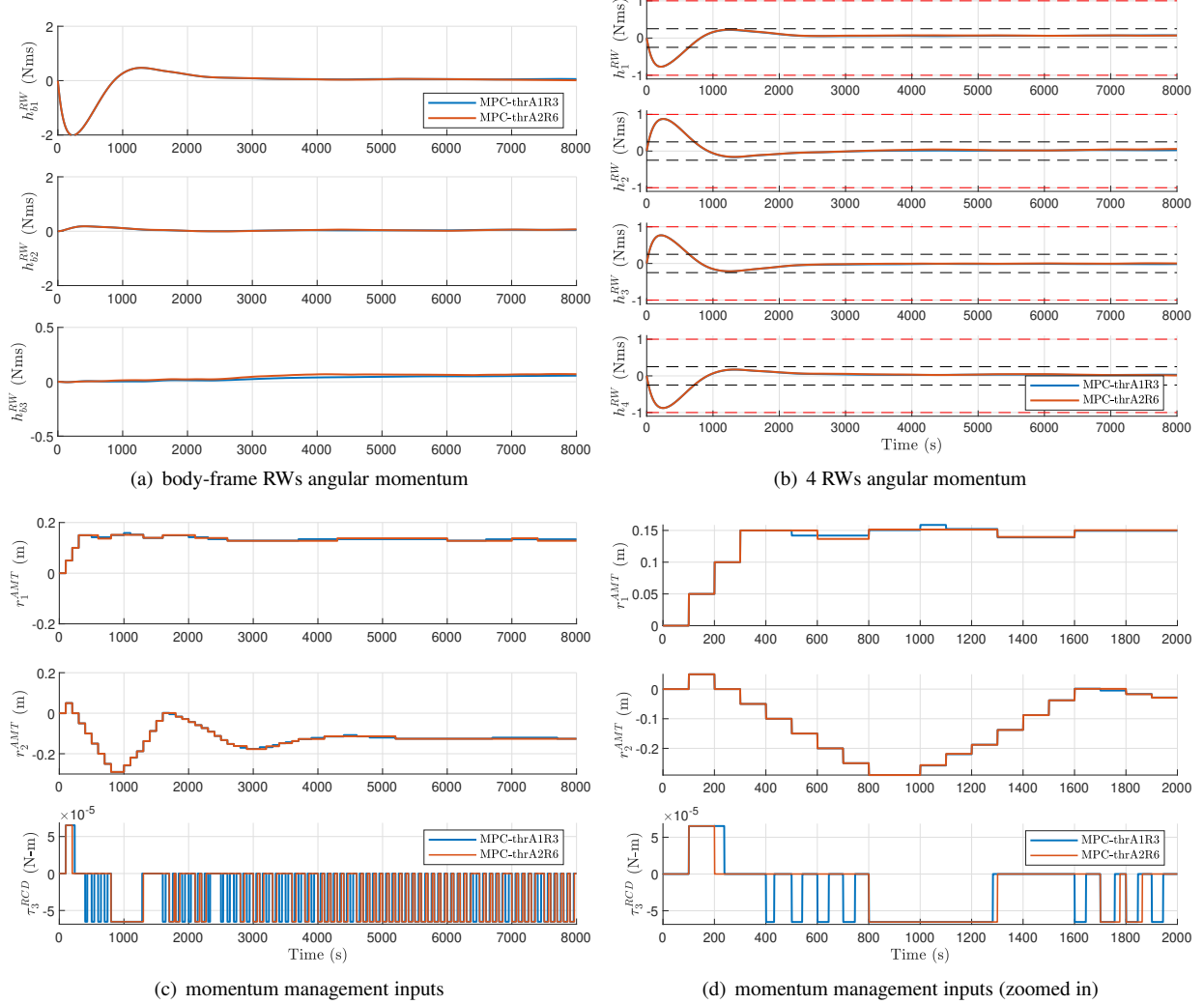


Figure 5: Threshold tuning using 10% AMT threshold and 30% RCD threshold (blue), and using 20% AMT threshold and 60% RCD threshold (red). The zoomed-in plot in (d) demonstrates the first 2000 seconds of slew maneuver and the PWM-quantized RCD actuation pulsing at every time step.

in momentum management performance. Leveraging the recursive nature of the MPC, an input activation threshold is applied to trim out minor actuation demanded by MPC, and further improve actuator efficiency and mitigate noise. A set of results are presented in Fig. 5, demonstrating the design choice of actuation thresholds. The result in blue (labeled “MPC-thrA1R3”) uses a 10% AMT threshold ($\beta_{\text{thresh}}^{\text{AMT}} = 0.1$) and 30% RCD threshold ($\beta_{\text{thresh}}^{\text{RCD}} = 0.3$), which means that when MPC demands an AMT input less than 10% of the distance the AMT can move in one direction in one time step (10% of 0.05 m), the AMT is held at its current position for the next time step, and the RCD input is set to zero when the MPC-demanded input is less than 30% of the RCD “on” torque value. The result in red (labeled “MPC-thrA2R6”) uses a 20% AMT threshold ($\beta_{\text{thresh}}^{\text{AMT}} = 0.2$) and 60% RCD threshold ($\beta_{\text{thresh}}^{\text{RCD}} = 0.6$) on the MPC-demanded inputs. Figures 5(a) and 5(b) show that the design choice of the applied thresholds do not degrade momentum management performance, which is further illustrated in the plot of the control inputs in Fig. 5(c) and the zoomed in control input plot of Fig. 5(d). A comparison of actuation usage among the the three MPC policies with different actuation threshold is included in Table 4. The performance metric of control actuation effort is evaluated by the number of RCD on-off cycles, the total time the RCDs are turned “on”, the total AMT travel distance in each translation axis, and the sum of the total AMT travel distance across both axes.

Figure 6 illustrates the disturbance torque estimates generated by the Kalman filter for the three MPC test cases. The black dashed lines are the true disturbances, accounting for the torque generated by the SRP due to the offset be-

Table 4: Momentum management control actuation usage of the proposed MPC policy under different actuation threshold tuning.

AMT/RCD Threshold	AMT 0% / RCD 0%	AMT 10% / RCD 30%	AMT 20% / RCD 60%
RCD Cycle (#)	74	69	48
RCD On Time (sec)	3850	3846	3593
AMT Dist 1 (cm)	33.85	24.21	26.33
AMT Dist 2 (cm)	100.11	95.50	93.43
Sum of AMT Dist (cm)	133.96	119.71	119.76

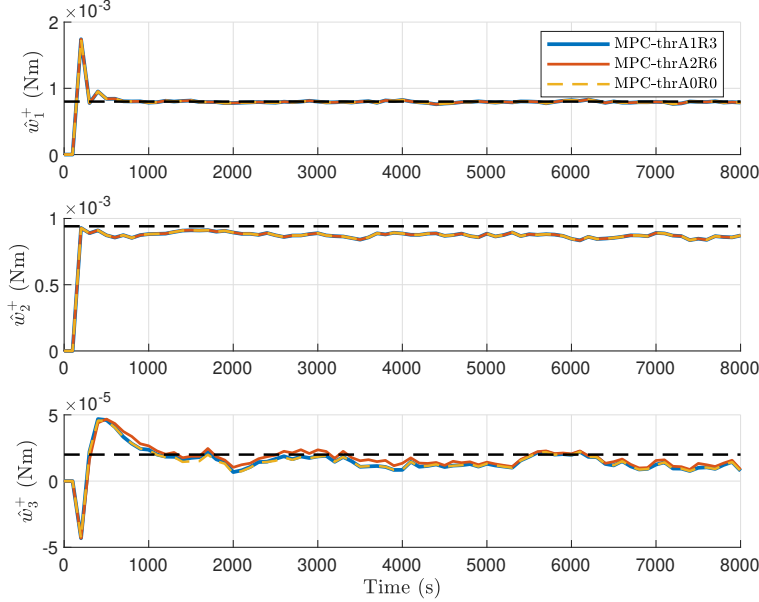


Figure 6: Kalman filter disturbance estimate values used in the MPC momentum management with 10% AMT and 30% RCD threshold (blue), 20% AMT and 60% RCD threshold (red), and no threshold (yellow).

tween the CM and CP. While the exact magnitude of the estimated disturbance torque does not exactly match the true disturbance torque, the estimate is reasonably accurate, and clearly assists with the MPC-based momentum management strategy, as shown in Fig. 4. It is worth noting that the disturbance torque estimate generated by the Kalman filter will account for all model inaccuracies in practice (e.g., nonlinearities, discretization approximations), which could explain the difference between the estimated and true disturbance torque.

5.4. State-of-the-Art Comparison

A 3° slew simulation is executed using the MPC framework to directly compare its actuation efficiency to that of NASA’s state-of-the-art method (Inness et al., 2023; Tyler et al., 2023). For this simulation, MPC uses the same tuning parameters as the simulations in Fig. 5 with 20% AMT threshold and 60% RCD threshold.

Figure 7 includes the comparison of simulation results using NASA’s method (Inness et al., 2023; Tyler et al., 2023) and the proposed MPC approach with thresholds. In Fig. 7(d), the MPC proactively actuates the AMT and RCDs to avoid angular momentum growth, as shown in Figures 7(b) and 7(c). A quantitative comparison of the control actuation usage is included in Table 5. The proposed MPC policy achieves a significant reduction in the total AMT travel distance. In contrast, the total RCD activation time is comparable between both methods. The PWM-quantization evenly distributes the input across every time step, as opposed to the longer singular “on” pulse with a long “off” period when using NASA’s benchmark method. Although the MPC results in higher RCD on-off cycles due to this inherent PWM quantization, dividing a long activation command into multiple short pulses is not inherently detrimental, as it mitigates the risk of potentially overheating the actuator associated with excessively long RCD “on” commands. Future work could investigate the design of an actuation mechanism capable of grouping these short MPC-generated pulses into a single, longer RCD activation event according to the mission requirements and hardware limitations.

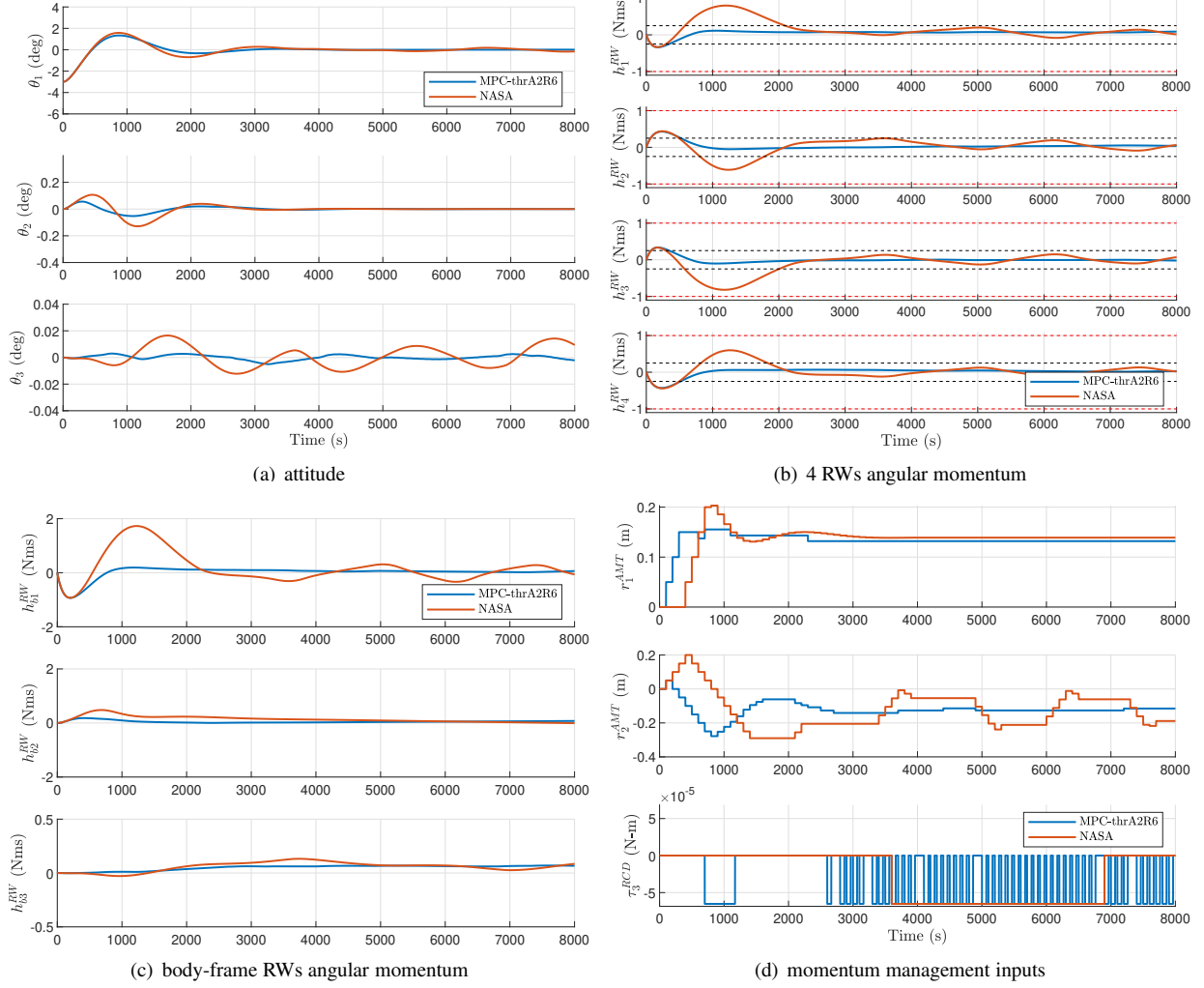


Figure 7: Comparison of simulation results using the proposed MPC momentum management strategy versus NASA’s state-of-the-art method under a 3° slew.

Table 5: Control effort usage with NASA’s state-of-the-art momentum management method and the proposed MPC method with 20% AMT and 60% RCD threshold under a slew from $\theta_0 = [-3^\circ \ 0 \ 0]^\top$ to $\theta_d = \mathbf{0}$.

Controller	NASA Solar Cruiser	MPC w/ Threshold
RCD Cycle (#)	1	49
RCD On Time (sec)	3300	3538
AMT Dist 1 (cm)	30.64	20.40
AMT Dist 2 (cm)	166.56	72.58
Sum of AMT Dist (cm)	197.20	92.98

6. Conclusions

This paper presented a novel Kalman filter augmented MPC framework specifically designed for the challenging momentum management task of NASA’s Solar Cruiser. The integrated estimation framework proposed in this work plays a crucial role, providing real-time state and disturbance estimates that not only characterize the external disturbance torque but also capture the dynamic discrepancies between the linear prediction model and the highly nonlinear spacecraft system. This estimate closes the modeling gap needed to enable model predictive control for this momentum management application. Building upon a previously-developed MPC architecture (Shen and Caverly, 2025b), the policy was rigorously formulated to be computationally feasible, utilizing off-the-shelf QP solvers to ensure real-time

implementation capability within the limited onboard hardware.

Simulation results demonstrated the proposed MPC-based momentum management policy's superior performance and robustness. The disturbance estimate was shown to be essential in achieving reliable MPC prediction and bounded momentum management. Furthermore, the proposed MPC policy successfully managed angular momentum growth under maneuvers that exceed the capability of NASA's state-of-the-art method designed for Solar Cruiser, establishing a larger operational slew envelope. The framework also proved its efficiency by demonstrating reduced actuator usage through a lower AMT travel distance and optimized RCD usage compared to the benchmark method. This improvement has the potential to enable greater solar sail mission longevity.

Future work on this topic could be the investigation of tracking larger, more dynamic slew maneuvers and the development of methodologies to proactively unload angular momentum in preparation for upcoming high-demand maneuvers. Additional work towards the implementation of the proposed method on flight hardware and software will also be pursued to move towards its implementation on future solar sail missions.

Acknowledgments

This material is based upon work supported by NASA under award No. 80NSSC25M7060, as well as a study grant from Chung Cheng Institute of Technology, National Defense University, Taiwan (R.O.C.).

References

Ahmed, Z., Halefom, M.H., Woolsey, C., 2024. Tutorial review of indirect wind estimation methods using small uncrewed air vehicles. *Journal of Aerospace Information Systems* 21, 667–683. doi:10.2514/1.I011345.

Bellar, A., Mohammed, M.A.S., Adnane, A., 2016. Minimum power consumption of the microsatellite attitude control using pyramidal reaction wheel configuration, in: 8th International Conference on Modelling, Identification and Control, pp. 253–257. doi:10.1109/ICMIC.2016.7804118.

Berthet, M., Schalkwyk, J., Çelik, O., Sengupta, D., Fujino, K., Hein, A.M., Tenorio, L., Cardoso dos Santos, J., Worden, S.P., Mauskopf, P.D., Miyazaki, Y., Funaki, I., Tsuji, S., Fil, P., Suzuki, K., 2024. Space sails for achieving major space exploration goals: Historical review and future outlook. *Progress in Aerospace Sciences* 150, 101047.

Boni, L., Bassetto, M., Niccolai, L., Mengali, G., Quarta, A.A., Circi, C., Pellegrini, R.C., Cavallini, E., 2023. Structural response of helianthus solar sail during attitude maneuvers. *Aerospace Science and Technology* 133, 108152. doi:<https://doi.org/10.1016/j.ast.2023.108152>.

Caverly, R., Di Cairano, S., Weiss, A., 2020. Electric satellite station keeping, attitude control, and momentum management by MPC. *IEEE Transactions on Control Systems Technology* 29, 1475–1489. doi:10.1109/TCST.2020.3014601.

Chen, T.Z., Liu, X., Cai, G.P., You, C.L., 2023. Attitude and vibration control of a solar sail. *Advances in Space Research* 71, 4557–4567. doi:10.1016/j.asr.2023.01.039.

Di Cairano, S., Kolmanovsky, I., 2018. Real-time optimization and model predictive control for aerospace and automotive applications, in: American Control Conference, pp. 2392–2409. doi:10.23919/ACC.2018.8431585.

Eren, U., Prach, A., Koçer, B., Raković, S., Kayacan, E., Açıkmese, B., 2017. Model predictive control in aerospace systems: Current state and opportunities. *Journal of Guidance, Control, and Dynamics* 40, 1541–1566. doi:10.2514/1.G002507.

Farres, A., 2023. Propellant-less systems, in: Branz, F., Cappelletti, C., Ricco, A.J., Hines, J.W. (Eds.), *Next Generation CubeSats and SmallSats*. Elsevier, pp. 519–541. doi:10.1016/C2020-0-00508-6.

Farrés, A., Heiligers, J., Miguel, N., 2019. Road map to l_4/l_5 with a solar sail. *Aerospace Science and Technology* 95, 105458. doi:<https://doi.org/10.1016/j.ast.2019.105458>.

Firuzi, S., Gong, S., 2018. Attitude control of a flexible solar sail in low Earth orbit. *Journal of Guidance, Control, and Dynamics* 41, 1715–1730. doi:10.2514/1.G003178.

Fu, B., Eke, F.O., 2015. Attitude control methodology for large solar sails. *Journal of Guidance, Control, and Dynamics* 38, 662–670. doi:10.2514/1.G000048.

Gauvain, B.M., Tyler, D.A., 2023. A solar sail shape modeling approach for attitude control design and analysis, in: 6th International Symposium on Space Sailing, New York, NY.

Halverson, R., Weiss, A., Lundin, G., Caverly, R., 2025. Autonomous station keeping of satellites in areostationary Mars orbit: A predictive control approach. *Acta Astronautica* 230, 1–15. doi:10.1016/j.actaastro.2025.01.064.

Hayes, A.D., Caverly, R.J., 2025. Atmospheric-density-compensating model predictive control for targeted reentry of drag-modulated spacecraft. *Journal of Guidance, Control, and Dynamics* 48, 2541–2556. doi:10.2514/1.G008665.

Heaton, A., Artusio-Glimpse, A., 2015. An update to the NASA reference solar sail thrust model, in: AIAA SPACE Conference and Exposition, Pasadena, CA. doi:10.2514/6.2015-4506. AIAA 2015-4506.

Heaton, A., Ramazani, S., Tyler, D., 2023. Reflectivity control device (RCD) roll momentum management for Solar Cruiser and beyond, in: 6th International Symposium on Solar Sailing, New York, NY.

Hibbert, L.T., Jordaan, H.W., 2021. Considerations in the design and deployment of flexible booms for a solar sail. *Advances in Space Research* 67, 2716–2726. doi:10.1016/j.asr.2020.01.019.

Huang, X., Zeng, X., Circi, C., Vulpetti, G., Qiao, D., 2021. Analysis of the solar sail deformation based on the point cloud method. *Advances in Space Research* 67, 2613–2627. doi:10.1016/j.asr.2020.05.008.

Inness, J., Diedrich, B., Valdez, B., Tyler, D., Sanders, B., 2024. Controls modeling approach for deployment of a large thin structures for solar sails, in: 38th Annual Small Satellite Conference, Logan, UT.

Inness, J., Tyler, D., Diedrich, B., Ramazani, S., Orphee, J., 2023. Momentum management strategies for Solar Cruiser and beyond, in: 6th International Symposium on Space Sailing, New York, NY.

Ismail, Z., Varatharajoo, R., 2010. A study of reaction wheel configurations for a 3-axis satellite attitude control. *Advances in Space Research* 45, 750–759. doi:10.1016/j.asr.2009.11.004.

Johnson, L., Curran, F., 2020. Solar Cruiser Technology Maturation Plans. Technical Report 20205003681. NASA Marshall Space Flight Center.

Johnson, L., Curran, F., Dissly, R., Heaton, A., 2019. The Solar Cruiser mission: Demonstrating large solar sails for deep space missions, in: International Astronautical Congress, Washington, DC.

Johnson, L., Everett, J., McKenzie, D., Tyler, D., Wallace, D., Newmark, J., Turse, D., Cannella, M., Feldman, M., 2022. The NASA Solar Cruiser mission - solar sail propulsion enabling heliophysics missions, in: 36th Annual Small Satellite Conference.

Lee, J.H., Kim, D., Kim, J., Oh, H.S., 2017. Shorter path design and control for an underactuated satellite. *International Journal of Aerospace Engineering* 2017, 8536732. doi:10.1155/2017/8536732.

Lee, S., Bunker, K.R., Caverly, R.J., 2025. CABLESSail: Solar sail momentum management using cable-actuated shape control. 7th International Symposium on Space Sailing .

Leve, F.A., Hamilton, B.J., Peck, M.A., 2015. Spacecraft Momentum Control Systems. Space Technology Library, Springer, Cham, The Netherlands.

Macdonald, M., McInnes, C., 2011. Solar sail science mission applications and advancement. *Advances in Space Research* 48, 1702–1716.

Markley, F.L., Crassidis, J.L., 2014. Fundamentals of spacecraft attitude determination and control. Space Technology Library, Springer, New York, NY.

Miller, D., Duvigneaud, F., Menken, W., Landau, D., Linares, R., 2022. High-performance solar sails for interstellar object rendezvous. *Acta Astronautica* 200, 242–252. doi:10.1016/j.actaastro.2022.07.053.

Orphee, J., Diedrich, B., Stiltner, B., Heaton, A., 2018. Solar torque management for the Near Earth Asteroid Scout CubeSat using center of mass position control, in: AIAA Guidance, Navigation, and Control Conference, Kissimmee, Florida. p. 1326. doi:10.2514/6.2018-1326.

Pezent, J.B., Sood, R., Heaton, A., Miller, K., Johnson, L., 2021. Preliminary trajectory design for NASA's Solar Cruiser: A technology demonstration mission. *Acta Astronautica* 183, 134–140. doi:10.1016/j.actaastro.2021.03.006.

Shen, P.Y., Caverly, R., 2025a. Solar Cruiser momentum management using model predictive control, in: 7th International Symposium on Space Sailing, Delft, The Netherlands.

Shen, P.Y., Caverly, R., 2025b. Solar sail momentum management with mass translation and reflectivity devices using predictive control. arXiv preprint arXiv:2503.12643.

Tyler, D., Diedrich, B., Gauvain, B., Inness, J., Heaton, A., Orphee, J., 2023. Attitude control approach for Solar Cruiser, a large, deep space solar sail mission, in: AAS Guidance, Navigation and Control Conference, Breckenridge, CO.

Vatankhahghadim, B., Damaren, C.J., 2021. Solar sail deployment dynamics. *Advances in Space Research* 67, 2746–2756. doi:10.1016/j.asr.2020.03.029.

Wang, J., Cheng, Z., He, G., Yuan, H., 2025. Uncertainty characterization of solar sail thrust with a multiscale modeling method. *Advances in Space Research* 75, 5640–5655. doi:10.1016/j.asr.2025.01.026.

Wie, B., 2004. Solar sail attitude control and dynamics, part 2. *Journal of Guidance, Control, and Dynamics* 27, 536–544. doi:10.2514/1.11133.

Woodbury, D., Junkins, J., 2010. On the consider Kalman filter, in: AIAA Guidance, Navigation, and Control Conference, p. 7752. doi:10.2514/6.2010-7752.

Zenere, A., Zorzi, M., 2018. On the coupling of model predictive control and robust Kalman filtering. *IET Control Theory & Applications* 12, 1873–1881. doi:10.1049/iet-cta.2017.1074.